Revised Proof

Dynamic atmospheric mechanisms associated with the diurnal cycle of hydrometeors and precipitation in the Andes–Amazon transition zone of central Peru during the summer season

Elver Villalobos-Puma[1,5,*] , Annareli Morales[2], Daniel Martinez-Castro[1],
Jairo Valdivia[3], Rodolfo Cardenas-Vigo[4], Waldo Lavado-Casimiro[5] and
Alexzander Santiago[1]

[1]*Instituto Nacional de Investigación en Glaciares y Ecosistemas de Montaña (INAIGEM), Lima, Peru.*
[2]*National Ocean and Atmospheric Administration (NOAA), Cooperative Institute for Research in Environmental Sciences (CIRES), University of Colorado-Boulder, Boulder, CO, USA.*
[3]*Instituto Geofísico del Perú (IGP), Lima, Peru.*
[4]*Instituto de Investigación de la Amazonía Peruana (IIAP), Dirección de Investigación de Información y Gestión del Conocimiento (GESCON), Iquitos, Peru.*
[5]*Universidad Nacional Agraria La Molina (UNALM), Programa de Doctorado en Recursos Hídricos, Lima, Peru.*
*Corresponding author. e-mail: evillalobos@inaigem.gob.pe

The diurnal cycle of total hydrometeor availability and its associated patterns of atmospheric circulation is studied over a connected Andes–Amazon (A–A) system in the central region of Peru during the summer season. Surface precipitation depends on the amount of hydrometeors that occur in the atmosphere and its atmospheric dynamics. Hydrometeors and the precipitation efficiency index were estimated using radar of the core satellite of the GPM system (N-GPM) for the period 2014–2022. The atmospheric dynamics were analyzed using the regional Weather Research and Forecasting (WRF) model. According to the results, the Andes mountain range produces precipitation at a surface level more efficiently during the afternoon and early evening hours (12–19 LT) due to the convergence of the thermal mesoscale circulations transporting moisture fluxes from the east and west. Both generate convective multicells along the Andes mountain range. The circulation from the west intensifies during the day, causing the displacement of the chain of convective multicells towards the east and producing hydrometeors and intense precipitations in the inter-Andean valleys. The A–A transition zone is more efficient in producing precipitation during the early hours of the day (00–07 LT) due to an increase in the northern circulation associated with the low-level jets and a change in the magnitude of the horizontal winds. Northerly winds enter the A–A transition zone with increased intensity and leave with reduced intensity. This mechanism is driven by the effect of the topographical barrier and the masses of cold air located in high areas on the eastern flank of the Andes. These factors generate significant updrafts and, therefore, the formation of storm clouds with high concentrations of hydrometeors and precipitation on the surface.

Keywords. Hydrometeors; precipitation efficiency index; precipitation; thermal circulations; Andes–Amazon connection system.

1. Introduction

The Andes–Amazon (A–A) transition region is considered one of the largest biodiversity hotspots on Earth (Myers *et al.* 2000). The sustainability and conservation of glaciers and water resources within the Andes along this transition region are modulated by the topography and the atmospheric forcings that prevail at different temporal and spatial scales (Sierra *et al.* 2022).

Chavez and Takahashi (2017) showed that increased precipitation occurs at night at low elevations (1000 m) with significant moisture transport from South American Low Level Jets (SALLJ) and orographically-forced convergence. The SALLJ (850 hPa) in some atmospheric situations is associated with the conditions of severe events in the inter-Andean valleys and on the eastern flank of the Andes (Flores-Rojas *et al.* 2021). Surface flows and valley-mountain circulations also drive the recycling of moisture from the Amazon forests to the high slopes of the Andes, whose atmospheric conditions favor persistent windward cloudiness (Giovannettone and Barros 2009; Kumar *et al.* 2019; Sierra *et al.* 2022). These cloud patterns are modulated by the mountain range, as the Andes provide orographic lift regardless of the time of day. At night, two cold regions of cloudiness are located in the A–A transition region and during the day, a region of cloudiness is formed along the crest of the Andes and inter-Andean valleys (Giovannettone and Barros 2009; Villalobos-Puma *et al.* 2020). At a regional level, on the eastern flank of the Andes, a convergence process associated with meridional circulations occurs. This process that drives upward vertical movements is the main component contributing to moisture intrusion from the Amazon into the tropical Andes, including the A–A zone (Segura *et al.* 2020).

The most significant interaction between topography and moisture fluxes occurs at different spatial and temporal scales, preferentially on the eastern flank of the Andes. Precipitation hotspots occur in these more active regions (Espinoza *et al.* 2015b; Chavez and Takahashi 2017; Junquas *et al.* 2018), and the precipitation amount is sensitive to the humidity recycling process that occurs in the Amazon region, as it contributes more than 50% of the total accumulated precipitation at high elevations (Satyamurty *et al.* 2013). Precipitation is organized according to the orography and the diurnal cycle that predominates in this tropical region, while its precipitation regime responds mainly to convective and stratiform precipitation, in which the amount of daily precipitation represents 70% associated with convection processes and 30% with stratiform events (Chavez *et al.* 2017), both contributions are vital in sustaining regional water in the central Andes of Peru.

The impacts on regional water depend on the amount of water vapor that can be removed from the atmosphere through precipitation processes forming hydrometeors (rain, snow, hail). The production of these hydrometeors, especially snow, is extremely useful for the central Andes of Peru because it contributes to the increase of glacier mass in the Huaytapallana glacier mountain range. However, estimating the amount of condensed water available for precipitation is challenging as no specific instrumentation network is available. Likewise, understanding precipitation patterns on the surface at the diurnal scale has strong limitations due to the lack of diurnal measurements of the types of precipitation (liquid and solid) in high mountains. Previous studies of cases of extreme events have shown that the central Andes is influenced by moisture transport from the Pacific and the Amazon, where the inter-Andean valleys (Mantaro Valley) are regions of greater activity of associated convection to precipitation production (Martínez-Castro *et al.* 2019; Flores-Rojas *et al.* 2021). However, the spatial patterns of hydrometeor production and orographic precipitation associated with the intrusion of both moisture flows (west and east) at the mesoscale level are not well understood during the summer.

During severe events like electrical storms (diurnal), the meeting of two opposite flows (east and west) was observed (Martínez-Castro *et al.* 2019). In this case, the coupled westerly circulation between thermally induced sea breezes and upslope winds introduces moisture from the Pacific side. The intensification of this circulation is associated with deep convection in the inter-Andean valleys (Flores-Rojas *et al.* 2021). The regional water depends on the amount of water vapor that can be removed from the atmosphere through precipitation processes forming hydrometeors (rain, snow, hail). Therefore, it is proposed to study the production of precipitation and hydrometeors at a diurnal scale; for that, we attempt to quantify the efficiency of condensate production and how it relates to surface precipitation in complex terrain using Global Precipitation Mission (GPM) radar data. The objective of this research is to understand the production of hydrometeors (solid and

Revised Proof

J. Earth Syst. Sci. _####################_   Page 3 of 24   _####_

liquid phase) and precipitation, as well as their associated patterns of atmospheric dynamics at the mesoscale level during humid days in the Andes region and its connection with the A–A zone. For that, scientific questions are raised: What is the fraction of tropospheric water available both in the liquid phase and in the solid phase? What are the mesoscale atmospheric mechanisms that prevail in the areas of greatest efficiency in the production of hydrometeors and precipitation?

2. Data and methodology

2.1 *Study area*

The study area is the Andes mountain range and the eastern slopes of the Andes in central Peru within the A–A transition zone (figure 1). This region includes the Huaytapallana glacier, which serves as a source and reservoir of water for the Shullcas sub-basin and the city of Huancayo. Due to its proximity to the city of Lima, agricultural and livestock products are transported from these inter-Andean basins.

2.2 *In situ and satellite observation data*

Due to the lack of hourly precipitation measurements, daily precipitation from pluviometers of the National Service of Meteorology and Hydrology of Peru (SENAMHI) was used to characterize the surface precipitation whose precipitation data had quality control and served as a basis to construct the gridded precipitation product: Interpolated data SENAMHI's Climatological and Hydrological Observations (Aybar *et al.* 2020). The rain gauges are located on the transect shown in figure 1(a) and numbered from left to right as E1, E2, E3, ..., E10. The analysis period covers from 2005 to 2019. Stations with at least 90% of existing data were considered. Table 1 shows the altitudes and locations of the rain gauges.

The core satellite of the GPM system (N-GPM) contains two active sensors operating in the Ku (13.6 GHz) and Ka (35.5 GHz) bands. Scanning these radars generates a set of hydroclimatic variables, which are available globally from latitude 65°S to 65°N (Hou *et al.* 2014). The radar precipitation estimation algorithm has seen significant improvement with the Next Generation Global
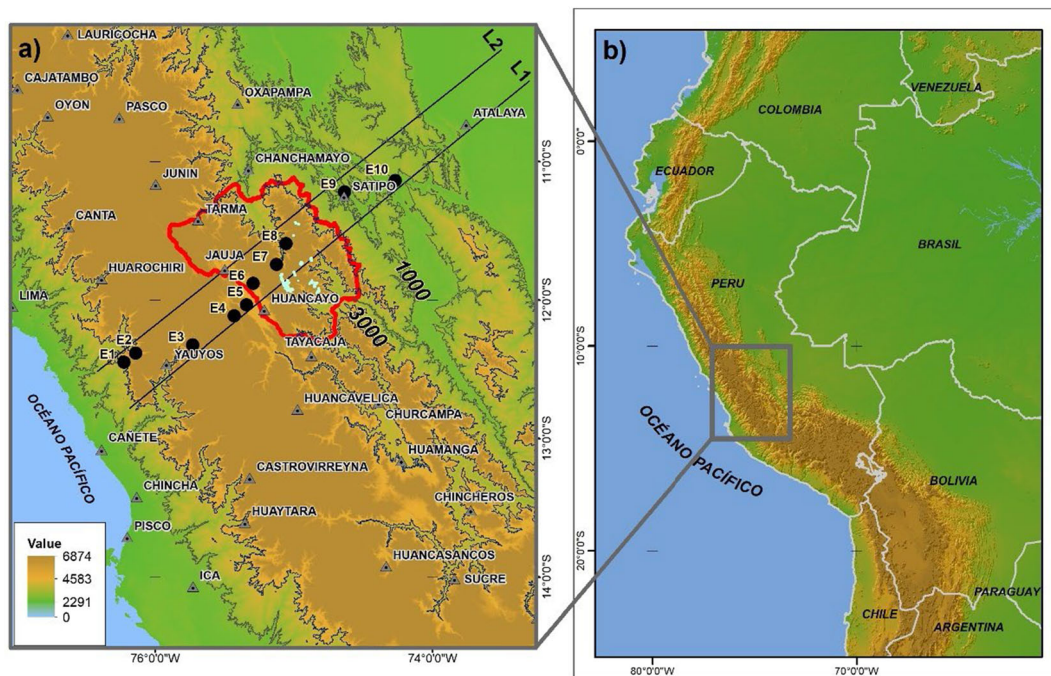

Figure 1. The Andes and the Amazon. (**a**) The red outline of the central mountain range of Peru and the Andes–Amazon transition zone is the Huaytapallana mountain range within which the glaciers are located (white color). The black points numbered from E1 to E10 are pluviometers distributed in the form of a transect (parallel to lines L1 and L2), the height contours at 1000 and 3000 m are provided for reference, and (**b**) the extension of the Andes at the level of Peru and neighboring countries.

Revised Proof

_####_   Page 4 of 24   *J. Earth Syst. Sci.* _####################_

Table 1. *Description of the pluviometric stations.*

	E1	E2	E3	E4	E5	E6	E7	E8	E9	E10
Lat. (°)	–12.45	–12.38	–12.33	–12.12	–12.04	–11.88	–11.75	–11.59	–11.22	–11.14
Lon. (°)	–76.22	–76.13	–75.72	–75.42	–75.34	–75.29	–75.12	–75.05	–74.63	–74.27
Alt. (m)	2600	3228	4675	3600	3360	3390	3640	3690	660	690

Precipitation Measurement (N-GPM). The combination of Ku and Ka wavelengths has allowed the estimation of microphysical parameters of clouds and precipitation, such as the mass-weighted mean diameter (Dm) and intercept parameter (Nw) of hydrometeors. This is a significant improvement over the precipitation radar of the Tropical Rainfall Measuring Mission (PR-TRMM) (Liao and Meneghini 2022). Using these microphysical parameters, the raindrop size distribution (DSD) can be estimated, and from the DSD, the equivalent reflectivity (Ze) and the precipitation rate (RR) can be obtained (Seto *et al.* 2013). For the analysis, we used version 7 of the N-GPM product. We utilized the Ku band 'Normal Scan' type scan, which consists of 49 beams (245 km) horizontally and 176 levels vertically. The spatial resolution was 125 m, and we gathered data during the period from 2014 to 2022.

Data from N-GPM was used to study the area, specifically two- and three-dimensional variables. These variables included Ze (dBZe) corrected for attenuation, RR (mm/hr) estimated in near-surface zones, Nw [1/mm6 mm], and Dm (mm). These variables relate to the concentration and representative size of the DSD. In addition, the liquid (LWP, kg/m^2) and solid (IWP, kg/m^2) water paths were used. LWP and IWP represent the total amount of precipitation particles (rain, snow, graupel-hail) integrated in the tropospheric column from a height near the surface (approx. 1–2 km) to the cloud top. For the central region of Peru, there is an evaluation of the N-GPM products, specifically the DSD and Ze variables, in three dimensions, which were discussed by Castillo-Velarde *et al.* (2021) and Valdivia *et al.* (2022). Taking these experiences into account, the N-GPM products were used for our study area.

2.3 *Methodology*

2.3.1 *Calculation of precipitation efficiency index from N-GPM*

Precipitation efficiency (PE, %) is defined as the fraction between the precipitation that reaches the surface and the content of condensed water in the atmospheric column (Sui *et al.* 2020). PE is a physical parameter that depends on environmental and topographical conditions. In this study, PE was defined from an observational perspective using the concentration of hydrometeors, both in liquid phase and solid phase, which were estimated by the N-GPM satellite throughout the tropospheric column. Since the concentration of hydrometeors was used, the precipitation efficiency index (PEI) will be defined to distinguish it from the original definition (Huang and Chen 2019).

To define the PEI, the total liquid water path (LWP), total solid water path (IWP) and precipitation rate (RR) were used:

$$PP = LWP + IWP, \qquad (1)$$

$$PEI = \frac{RR}{PP} \times 100. \qquad (2)$$

In equation (2), to divide RR [mm/h] by PP [kg/m^2/h], it was considered that 1 kg/m^2 is equal to 1 mm of rain. The PEI quantifies the contribution of hydrometeors (LWP and IWP) that fall on the surface as precipitation. Higher values of PEI indicate regions containing hydrometeor clouds that generate greater production of surface precipitation (Huang and Chen 2019). To spatially visualize the PEI and other N-GPM variables, a regular grid map was created using swath scanning for both two- and three-dimensional with 0.05° horizontal resolution.

For each precipitation event, a simulation was carried out with the WRF model for 24 hours with hourly output. The simulation start time was considered to be at least 12 hours before the time the event was detected by the N-GPM. In this way, the 12 hours of spin-up of the model are guaranteed, which is consistent for simulations of precipitation events (Martínez-Castro *et al.* 2019). The atmospheric dynamics associated with precipitation events were processed for humid days with the presence of precipitating clouds (verified in the N-GPM scan). To analyze the mesoscale atmospheric dynamics, the variables obtained by the WRF model were grouped according to the time

Revised Proof

J. Earth Syst. Sci. _####################_   Page 5 of 24   _####_

and date of coincidence with the N-GPM scan time. Precipitation events were selected using the estimated surface reflectivity by the N-GPM; this variable is a good indicator to detect precipitation clouds and the concentration of hydrometeors; specifically, a threshold of Ze > 25 dBZe at the surface level was used. Therefore, it was not necessary to use the *in situ* records of precipitation; in addition, in the study region, there is not enough hourly data from the pluviometer to verify the precipitation estimated by the N-GPM.

2.3.2 *Model setup for a mesoscale simulation*

For the analysis of the mesoscale atmospheric dynamics associated with the occurrence of precipitation events identified by the N-GPM, the Weather Research and Forecasting (WRF) version 4.0 model (Skamarock *et al.* 2019) was used with the Advanced Research WRF (ARW) variant. The WRF-ARW model was used to simulate real cases of atmospheric processes of precipitation events based on physical equations used by the model for a compressible and non-hydrostatic atmosphere. The model was configured with the following physical parameterization schemes: Yonsei University Scheme (YSU) for the Planetary Boundary Layer (PBL), Morrison double-momentum for microphysical parameterization, Grell-Freitas scheme for convection parameterization (see table 2), and the RRTMG shortwave and longwave radiation schemes. This model configuration is consistent with previous sensitivity studies of physical parameterization schemes for different spatial resolutions that were carried out in the Andes Mountains, including the A–A region (Moya-Álvarez *et al.* 2018, 2019).

Downscaling was performed through one-way nesting, with spatial resolutions from 31 to 4 km (see table 2). The largest domain was initialized with ERA5 reanalysis boundary conditions every 6

hours and 31 km spatial resolution. For each range of the diurnal cycle in local time (LT) (08–11 LT, 12–15 LT, 16–19 LT, 20–23 LT, 00–03 LT, 04–07 LT), 20 precipitation events were simulated, obtaining a total of 120 simulations. The simulated events were selected from the events captured by the N-GPM satellite for the summer months (DJF) for the period 2014–2022. A precipitation event was considered when the estimated precipitation rate on the surface was greater than zero in the N-GPM radar swath.

3. Results

3.1 *Cross-sectional characterization of precipitation on a daily scale*

In the Andes region and the A–A transition, the average annual precipitation shows a significant variation along the transect (figure 1a). Annual precipitation (Ra) increases from the lower slopes located on the west side of the Andes to the highest regions of the Andes (E1–E3), then decreases as we move towards the inter-Andean valleys (E4–E6) but again increases as we move towards the Amazon regions (E7–E9), and finally, in E10, it decreases again. Throughout the transect, the highest Ra is found in E9, which corresponds to the A–A transition region. In the spring months (SON) and in the autumn (MAM), the contributions represent 20% of the Ra in the pluviometer stations from E4 to E10. While at stations E1–E3 (west slopes), a significant variation in contributions is observed; during the SON, the contribution is minimal at $\approx 5\%$, and in the MAM, its contribution is around 40%.

During the summer (black dots), the contribution represents $\approx 45\%$ in the transect (figure 2a); specifically, on the western slopes, there is an increase of up to 60% of Ra (E1–E2). Finally, the contribution during the months of higher humidity (November–April) has a pronounced negative slope

Table 2. *WRF model configuration.*

	Domain 1	Domain 2
Horizontal resolution	12 km	4 km
Boundary and initial conditions	ERA5 – 31 km	WRF – 12 km
Cumulus parameterization	Grell-Freitas scheme	None
Microphysical parameterization	Morrison double-momentum	Morrison double-momentum
Vertical resolution	45 levels (50 m, first level)	45 levels (50 m, first level)

along the transect. On the western slopes, the contribution to total Ra can reach values close to 100% (E1–E2); this value decreases as one advances towards the Amazon; however, there is a slight increase in E10 (figure 2a). It has been found that low contributions occur in the transition region A–A (E9) during the wet season, which indicates that in this region, the contribution to Ra is generated during the other months (dry months) with a significant percentage close to 30%.

Pa indicates the accumulated summer precipitation (figure 2b); its transverse behavior is similar to that of Ra (figure 2a) because summer precipitation contributes an average of 50% along the transect. The precipitations that occur with greater frequency (Pf) and intensity (Pi) are located in the transition regions A–A (E8–E9) and Andean regions of higher altitude (E3). These parameters (Pf and Pi) show two well-marked peaks with similar values of 4.5 mm/day at stations E3 and E9. In this last station, the 75th percentile of Pi is exceptional (12 mm/day), which represents an extreme value compared to other stations of the transect, and it is particularly evident that in this A–A transition region, intense precipitations with high variability occur during summer.

3.2 *Spatial distribution of tropospheric hydrometeors*

Total tropospheric hydrometeors show a significant contrast between the Andean and Amazon regions in both the solid and liquid phases (figure 3). The IWP (figure 3c) has higher values than the LWP in the Andean region; in addition, in these regions, very deep clouds occur that average above 10 km above sea level (figure 3e). This indicates that the Andean zone is mainly composed of solid-phase hydrometeors, while in the A–A and Amazon transition zones it is mainly composed of liquid-phase hydrometeors (figure 3c), although very deep clouds occur in specific areas (figure 3e) containing solid phase hydrometeors. The LWP extends from the Amazon to the interior of the Andes and enters through valleys located to the northeast and southeast of the Huaytapallana mountain range, favoring water availability for the generation of precipitation in the inter-Andean valley and highlands of the Andes. The IWP has significant values in the A–A transition zone, probably associated with very deep vertical development clouds mainly containing solid phase hydrometeors.

In a topographically complex area, it is important to visualize the radar blind zone as they can affect the estimation of precipitation variables by radar. In figure 3(d), the ravines that lead to the interior of the Andes are observed to have heights of 3 km as a blind zone, which indicates that it is not possible to capture the entire column of precipitation clouds due to the fact that the radar echo is strongly contaminated by the irregular topography of the Andes. However, in the A–A transition region, the blind zone does not have high values as in the ravines, which allows the radar to obtain information from heights very close to the surface and consequently favors a more realistic estimate of precipitation variables, especially in regions where the height of the blind zone is minimal, such as the Amazon region. On the other hand, the average PEI during wet days (figure 3f) has values over the A–A transition zone and in the streams that channel the PEI towards the interior of the Andes. This indicates that these zones are more effective in producing clouds with high concentrations of hydrometeors that generate
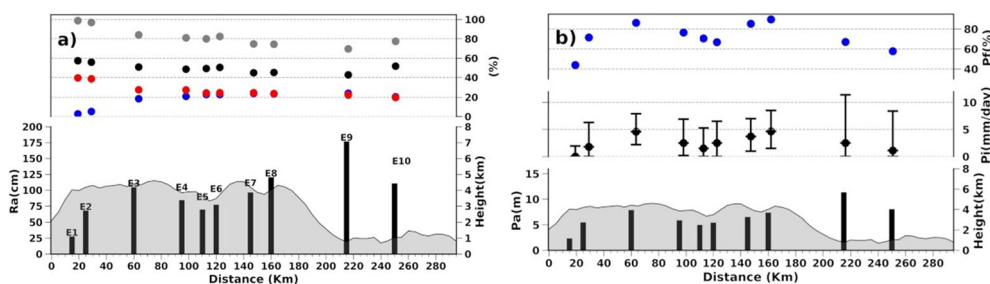

Figure 2. Variation of precipitation in the Andes and Amazon transect. (**a**) Annual precipitation (Ra, cm), colored dots indicate contributions (%) to annual rainfall. Blue and red colors correspond to SON and MAM transition stations, respectively; black represents the summer season (DJF), and gray is for the wet period (November–April). (**b**) Accumulated precipitation (Pa, m), intensity (Pi, mm/day) and frequency (Pf, %) for the months DJF of the period 2005–2019. Height (km) indicates the vertical profile of the topography of the Andes and the Andes–Amazon transition zone.
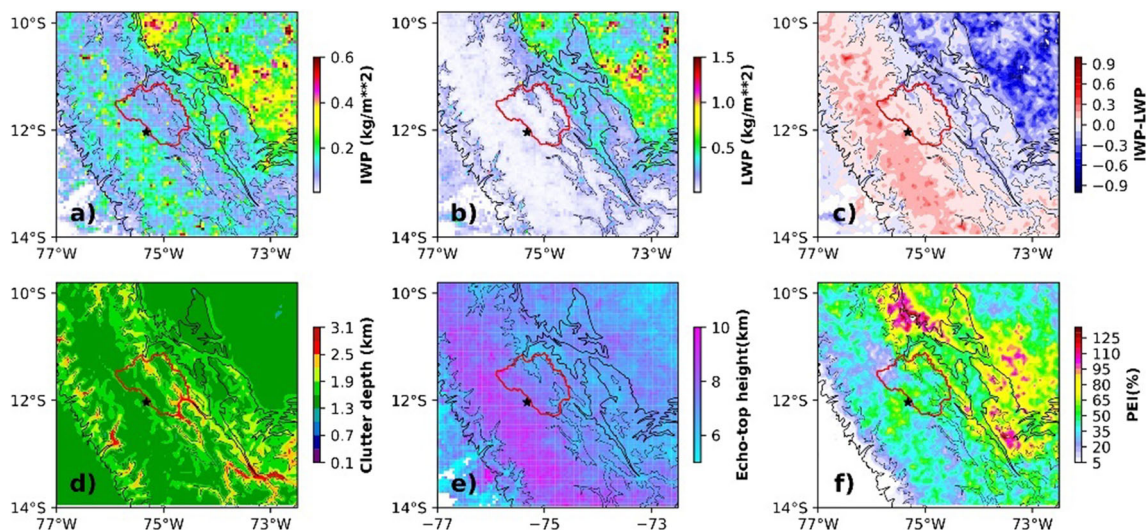
Figure 3. Tropospheric hydrometeors during the rainy period (DJF) calculated from N-GPM satellite, (**a**) solid phase hydrometeors (IWP, kg/m^2), (**b**) liquid phase hydrometeors (LWP, kg/m^2), (**c**) difference between IWP and LWP, (**d**) clutter depth (km), (**e**) echo-top height (km) of cloud system, and (**f**) precipitation efficiency index (PEI, %).

precipitation on the surface; likewise, regions with important PEI values are observed to the west of the Huaytapallana mountain range (red outline).

The PEI shows well-defined patterns during the diurnal cycle (figure 4); at some specific times, the patterns are different from the average daily values (figure 3), which shows that the diurnal cycle has a significant effect on the precipitation patterns in this study region. During the period from 08 to 11 LT, the PEI is more pronounced on the eastern side of the Huaytapallana mountain range, especially in the A–A transition zone. During the period from 12 to 15 LT, the spatial pattern of PEI changes significantly with more intense values on both sides of the Andes, as well as in the inter-Andean valleys. During the period from 16 to 19 LT, the PEI pattern is mainly concentrated in the western fringe of the Huaytapallana mountain range, covering the western slopes of the Andes above 3000 m a.s.l. Likewise, a small PEI hot-spot area located in the Mantaro Valley (black star) is observed. During the period from 20 to 23 LT, the PEI values decrease markedly in almost the entire region, except in the southern and northern areas. During the period from 00 to 03 LT, the PEI begins to increase again to the east and south of the Huaytapallana mountain range, and from 04 to 07 LT, the PEI values intensify notably, especially in the transition zone A–A and in an Amazonian strip that goes from the northwest to the southeast. These results show the spatial patterns of cloud development that generate surface precipitation. Also, it was found that during the day, the most

productive hours of hydrometeors and precipitation are between 12 LT and 19 LT. In the A–A transition zone, hydrometeors and precipitation are produced both during the day and at night, the peak being between the hours of 04 LT and 07 LT. Likewise, two opposite PEI patterns were found to occur between 16–19 LT and 04–07 LT, which shows that different atmospheric circulation mechanisms act at these specific times, which will be studied in section 3.4.

3.3 *Vertical structure of precipitation clouds*

The vertical structure of the precipitation cloud system is shown in figure 5. In the early hours of the day (08–11 LT), the bright band is observed on the western slopes of the Andes (figure 5a), indicating the occurrence of stratiform precipitation. In addition, in the inter-Andean zone, cumulus clouds that are probably in the formation phase are observed, while in the A–A transition region, the combination of both types of stratiform and convective clouds is observed. Deep clouds predominate in this region, with important convection nuclei associated with cumulonimbus clouds that reach heights close to 14 km above the surface. During the period from 12 to 15 LT, the predominant clouds are of the convective type (figure 5b) and are located in the higher mountainous regions compared to the previous times (08–11 LT). The same pattern is observed in the inter-Andean valleys; in addition, some convective clouds persist over the A–A transition region. In the following
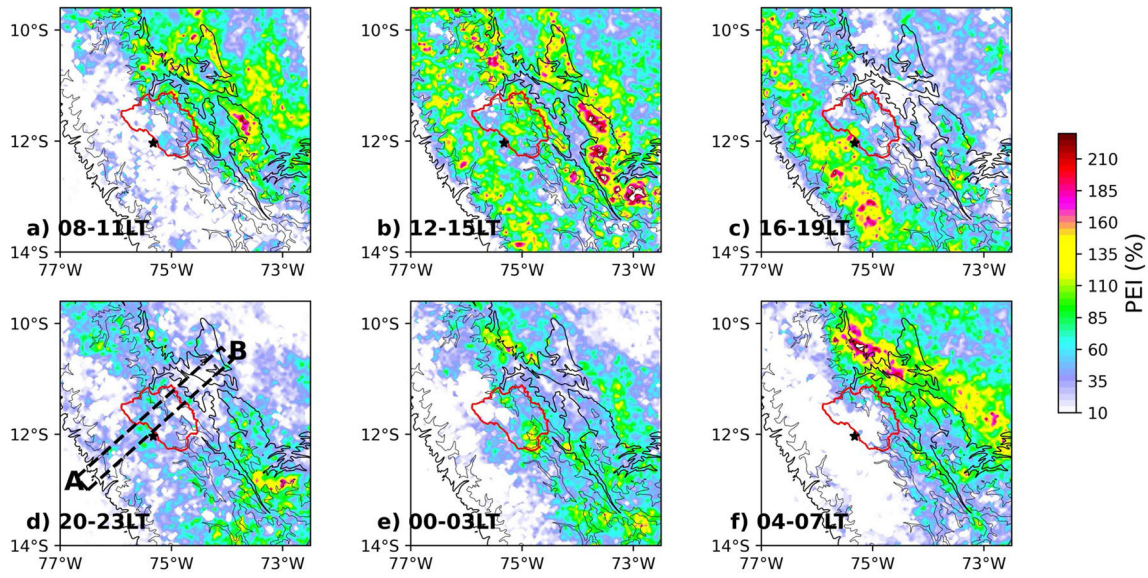
Revised Proof

_####_   Page 8 of 24   *J. Earth Syst. Sci.* _###################_

Figure 4. Diurnal cycle of precipitation efficiency index (PEI, %) during the rainy period (DJF), (**a**) 08–11 LT, (**b**) 12–15 LT, (**c**) 16–19 LT, (**d**) 20–23 LT, (**e**) 00–03 LT, and (**f**) 04–07 LT. Cross-section (A–B) in panel (d) will be used to represent the vertical structure of precipitating clouds (see section 3.3).
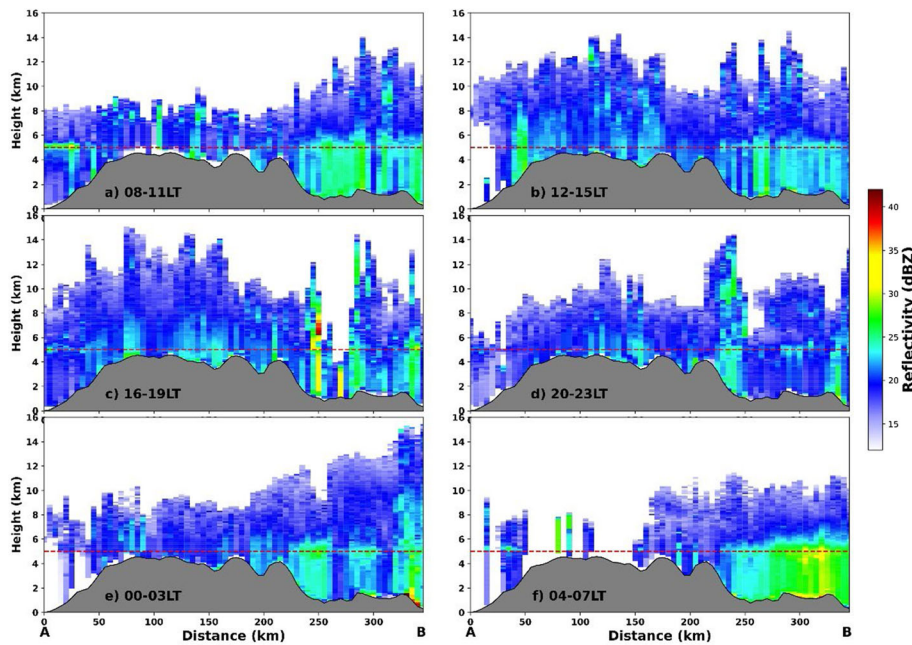

Figure 5. Diurnal cycle of precipitating cloud system calculated from N-GPM satellite during the rainy period (DJF), (**a**) 08–11 LT, (**b**) 12–15 LT, (**c**) 16–19 LT, (**d**) 20–23 LT, (**e**) 00–03 LT, and (**f**) 04–07 LT. See figure 4(d) for the map of the cross-section A–B. Gray shading represents topography, and the red line refers to the height of 5 km ASL.

period (16–19 LT) on the western slopes of the Andes, the structure of the precipitation clouds shows the presence of a bright band (Kumar *et al.* 2019; Villalobos *et al.* 2019), it indicates that the precipitation clouds are in the process of dissipation.

In contrast, in the inter-Andean valleys, convective activity persists. Subsequently, the intense convection dissipates rapidly in hours (20–23 LT

and 00–03 LT, figure 5d and e) (Chavez *et al.* 2017; Villalobos-Puma *et al.* 2020). In the Andean regions, the dissipation of precipitation clouds is characterized by not having a defined bright band; this is due to the fact that the radar has limitations in detecting the complete structure of the clouds due to the height effect of the blind zone, which is explained in section 3.2. On the eastern slopes of the Andes (figure 5c), convective clouds are

observed, especially in the A–A transition zone. Later, during the early night hours (20–23 LT), the storm clouds move towards the upper areas of the slopes to the east of the Andes (figure 5d). During the period from 00 LT to 03 LT, a change in the vertical structure of the precipitation clouds is observed due to the dissipation process, and from 04 LT to 07 LT, the clouds completely dissipate over the Andes. Instead, at the far right of the A–A transition zone (figure 5e), convective clouds begin to intensify and reach heights of 15 km above the surface (Chavez and Takahashi 2017). During the period from 04 to 07 LT, the convective clouds begin to dissipate, forming stratiform-type clouds (figure 5f). Likewise, it is observed that the clouds cover the higher mountain areas with low reflectivity values, probably generating snow precipitation. These precipitations on higher slopes are strongly influenced by the precipitation system that occurs with high PEI values (figure 4f) in the lower areas of the Andes–Amazon transition zone.

The total hydrometeor transects (IWP and LWP) and the cloud top echo show changes according to the diurnal cycle. In general, the clouds are deeper over the Andes than the Amazon, and the decay of their height occurs in the A–A transition zone (figure 6) in response to the topographic gradient. In figure 6(a), it is observed that a greater quantity of hydrometeors is produced in the A–A transition region and over the Amazon compared to those generated over the Andes. Over the Andean region, the IWP exceeds the LWP values, and over the Amazon, this relationship is inverted (figure 6); this result is consistent with the spatial distribution of hydrometeors shown in figure 3. High LWP values observed over the A–A transition region and over Amazonia respond to the presence of precipitation clouds that are generated more frequently in an environment with a warm atmosphere, which is below freezing height. A clear example is observed in figure 6(f); the highest value of LWP corresponds to the stratiform clouds (figure 4f) that are observed in transition zone A–A. Over the Andean region, the predominant fraction is of the solid type (IWP) due to the fact that the predominant cloud cover is above or close to the freezing height, in which an environment with a cold atmosphere predominates (Valdivia *et al.* 2022).

In figure 7, the total number of hydrometeors (PP) and the PEI are shown. During the period from 08 to 11 LT, there is an important gradient of PEI in a west–east direction, the same pattern is

seen in PP but to a lesser extent. On the western slopes of the Andes, the PP is higher than the PEI, which indicates that there is a high availability of precipitation particles in the troposphere. However, not enough precipitation occurs at the surface level. During the period from 12 to 15 LT, the PEI increases significantly over the Andes compared to the previous period (08–11 LT). The most effective areas in the production of clouds and precipitation are located on the crests and slopes of the mountains on both sides of the mountain range. Instead, the PP values are relatively uniform throughout the entire transect. During the period from 16 to 19 LT, higher PEI values are observed over the Andes, while over the A–A transition region, the intensity of PEI values falls sharply. This result indicates that during this period, there is sufficient cloudiness and precipitation on the surface over the Andes compared to the A–A transition area, and consequently, a PEI gradient in an east–west direction is generated. During 20–23 LT and 00–03 LT, the PEI values decrease considerably throughout the transect. However, during the 00–03 LT, important PEI signals begin to generate on the A–A transition zone. At the right end of the transect, on the low hills, the PP values exceed those of PEI, which indicates that a sufficient amount of precipitation particles are produced; however, these hydrometeors do not reach surface levels (figure 7e). During the period from 04 to 07 LT (figure 7f), higher PEI values are observed in the Amazon and the A–A transition zone, while, over the Andes, PEI values are close to zero. It was found that PEI exhibits distinct patterns along the transect. Furthermore, two opposite patterns of PEI, with positive (figure 7f) and negative (figure 7c) gradients, were found in the transect. The possible causes of these patterns will be discussed in later sections (3.4 and 3.5).

3.4 *Mesoscale atmospheric flows*

Figure 8 shows the surface moisture flux as a function of slope; this variable allows us to understand the local surface circulation influenced by valley-mountain conditions. During the day, surface flows upslope predominate, and at night, downslope predominate (Junquas *et al.* 2018). In general, the surface moisture flow of the upslope type intensifies during the daytime (figure 8b) on both sides of the mountain range, which is induced by thermal circulation forced by solar radiation
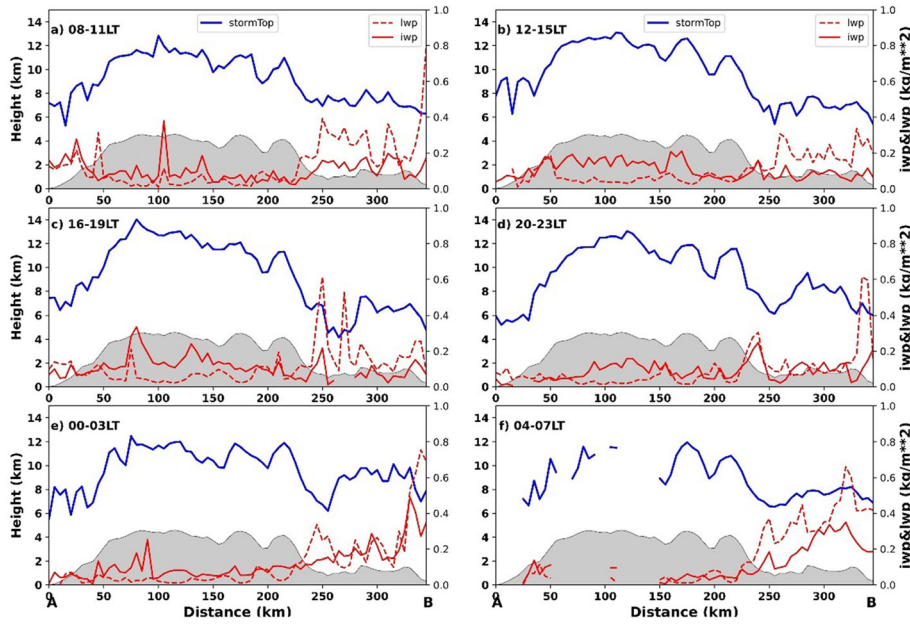
Figure 6. Similar to figure 5, but for total tropospheric hydrometeors (red dashed line is LWP, solid red line is IWP) and cloud top (blue line). (**a**) 08–11 LT, (**b**) 12–15 LT, (**c**) 16–19 LT, (**d**) 20–23 LT, (**e**) 00–03 LT, and (**f**) 04–07 LT.
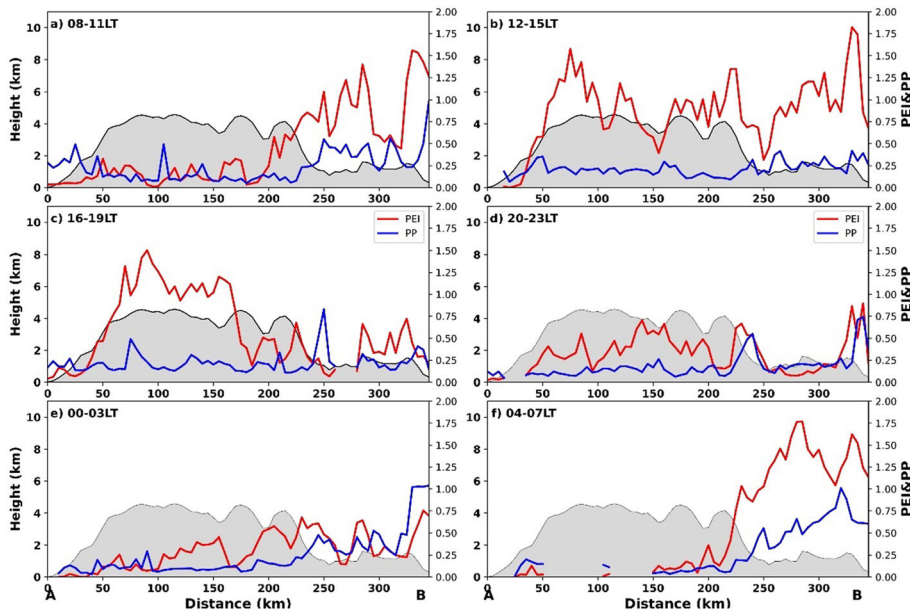

Figure 7. Same as figure 6, but for PEI (red solid line) and PP (blue solid line).

incident on the slopes. In addition, it is evident that when the magnitudes of moisture fluxes intensify, a pronounced development of precipitation clouds is generated. For example, in the afternoon hours (12–19 LT), when the PEI (figure 4b and c) has higher values over the Andes mountain range, the flows from the western slopes intensify and manage to enter the inter-Andean valleys, favoring the production of clouds and precipitation at surface level. At night, the direction of the flows is reversed in relation to daytime flows, showing downslope-type flows. This behavior occurs predominantly in the valleys on the eastern side of the Huaytapallana mountain range (figure 8d, e and f). This behavior indicates that the mountain-to-valley circulation is significant over the streams in the transition zone A–A. These air masses that descend from the high areas have low temperatures and accumulate in the valleys and ravines. These cold westerly winds at a
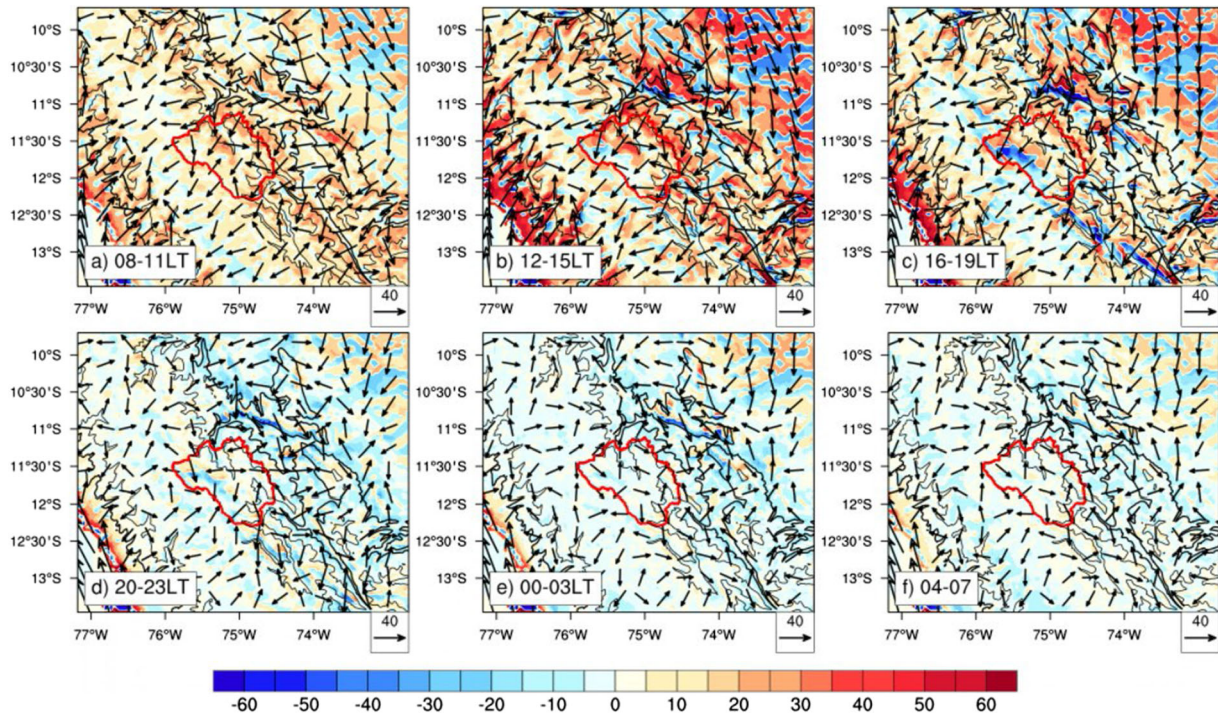
Figure 8. Surface flux of moisture ($uq[dz/dx + dz/dy]/$sqrt$(dz/dx * dz/dx + dz/dy * dz/dy)$) associated with upslope (positive values) and downslope (negative values) components determined from WRF simulations for precipitation events during summer (DJF), where reference vector (the lower right corner) has unit: g/kg $*$ m/s, the red contour is the Huaytapallana mountain range. (**a**) 08–11 LT, (**b**) 12–15 LT, (**c**) 16–19 LT, (**d**) 20–23 LT, (**e**) 00–03 LT, and (**f**) 04–07 LT.

mountain-valley scale play an important role during the early morning hours because when they interact with northeasterly flows, they promote pronounced convergence in the Andes–Amazon transition zone (Giovannettone and Barros 2009; Chavez and Takahashi 2017). This statement is discussed in more depth in section 3.5 using figure 11.

The $IVT_{sfc–500\ hPa}$ (figure 9) indicates the transport of water vapor across the transition zone A–A. It is observed that the transport of water vapor occurs in north and northwest directions, following the contour of the topography of the eastern side of the Andes. Likewise, the intensity of $IVT_{sfc–500\ hPa}$ shows varying patterns during the diurnal cycle. Early in the morning (08–11 LT), the flows enter the Andes through the ravines. These flows intensify at 12–15 LT, increasing water vapor transport in the A–A transition zone. In turn, these flows enter the inter-Andean valleys through the ravines located to the north and south of the Huaytapallana mountain range. The water vapor transport persists during the following hours (16–19 LT) without significant variations. At this time of day (12–19 LT), when the transport of water vapor flow intensifies in the A–A transition zone, consequently, precipitation patterns increase strongly

along the Andes mountain range (figure 4b and c). During the period from 20 to 23 LT, the magnitude of $IVT_{sfc–500\ hPa}$ decreases notably in the ravines on the eastern side of the Andes. During the period from 00 to 03 LT, $IVT_{sfc–500\ hPa}$ presents higher intensities compared to the other periods of the day, particularly intensifying in the ravines of the transition zone A–A. Finally, during the period from 04 to 07 LT, the $IVT_{sfc–500\ hPa}$ decreases over the entire study region. At night (00–07 LT), increased precipitation occurs in transition zone A–A as water vapor flow intensifies (figure 4e and f).

The $IVT_{500–200\ hPa}$ (figure 10) is conditioned by the easterly circulation during 24 hours of the day due to the influence of Alta Bolivia. Meanwhile, its intensity changes depending on the diurnal cycle. During the period from 08 to 11 LT, an increase in the intensity of $IVT_{500–200\ hPa}$ is observed over the transition zone A–A and the Amazon. During the period from 12 to 15 LT, the intensity of $IVT_{500–200\ hPa}$ decreases slightly in the transition zone A–A. During periods 16–19 LT and 20–23 LT, the intensity of $IVT_{500–200\ hPa}$ again increases to the north and south of the Huaytapallana mountain range and over the highlands of the Andes (west of the Huaytapallana mountain range).
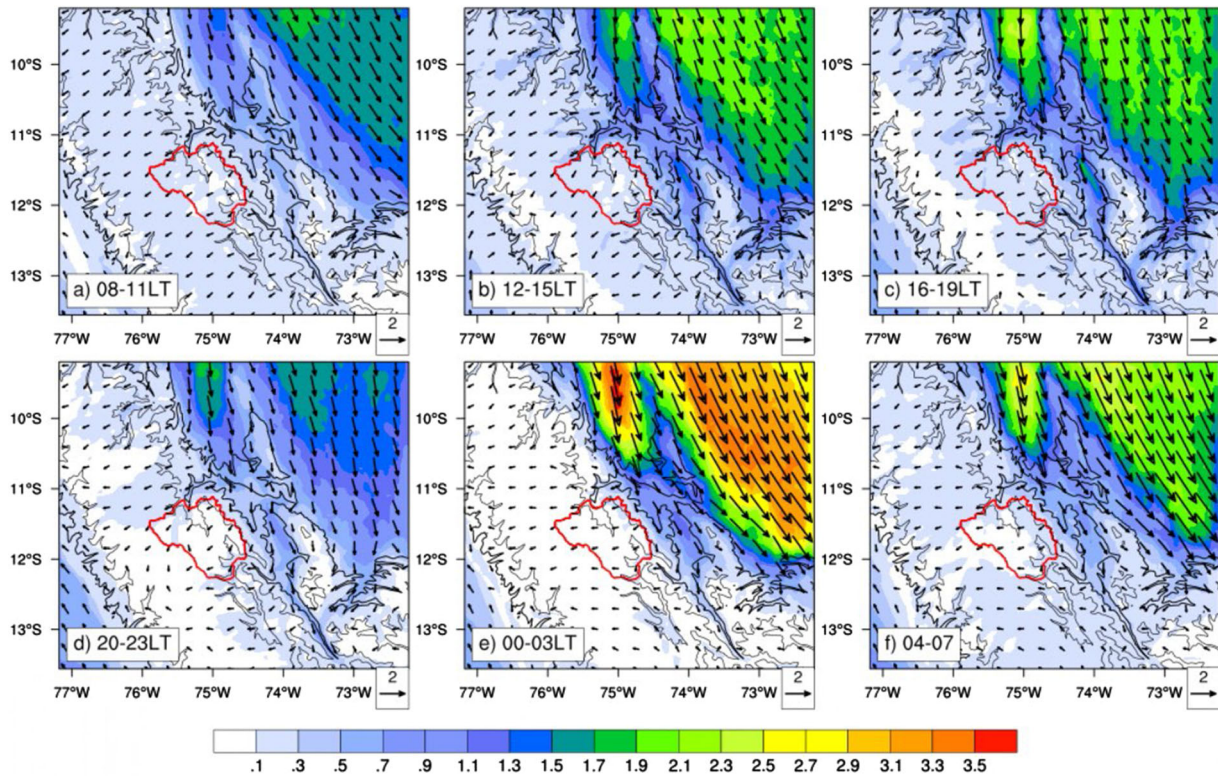
Revised Proof

_####_   Page 12 of 24   *J. Earth Syst. Sci.* _####################_

Figure 9. Diurnal cycle of integrated vapor transport ($IVT_{sfc-500\ hPa}$, kg m^{-1} s^{-1}) between the surface level and 500 hPa of the troposphere from WRF simulations for precipitation events during summer (DJF). (**a**) 08–11 LT, (**b**) 12–15 LT, (**c**) 16–19 LT, (**d**) 20–23 LT, (**e**) 00–03 LT, and (**f**) 04–07 LT.
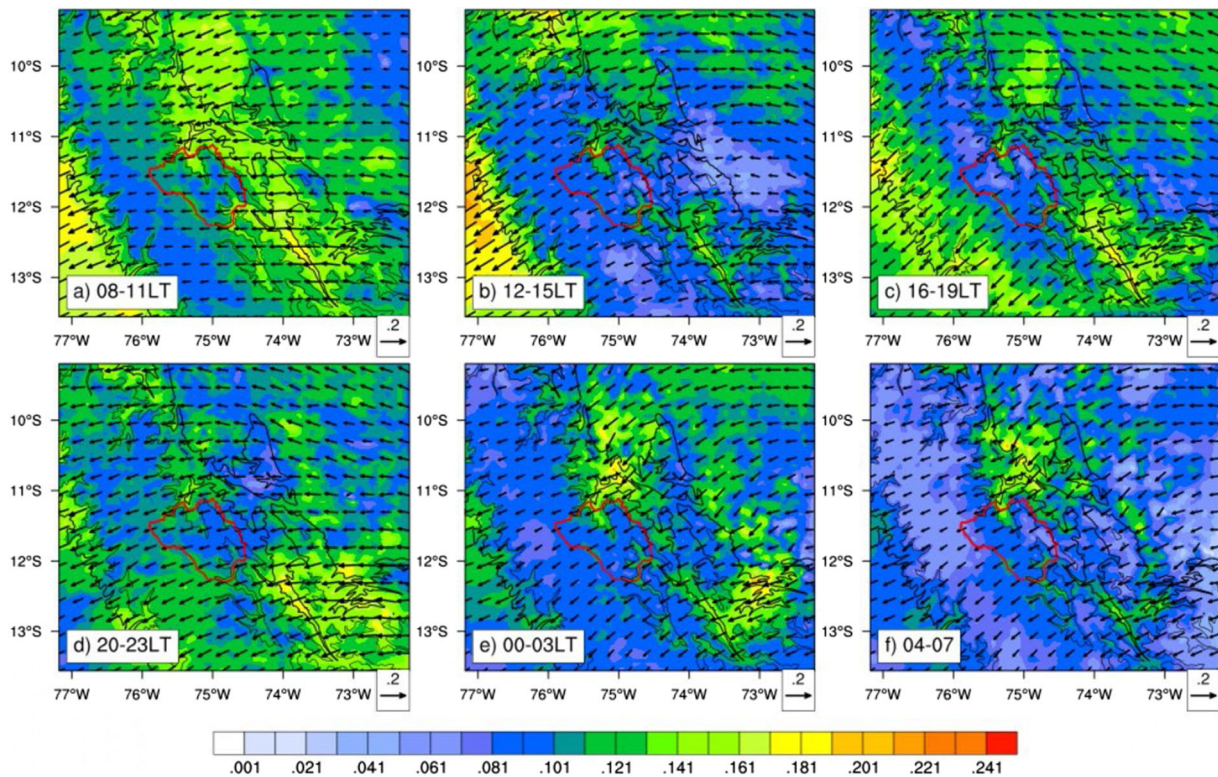

Figure 10. Similar to figure 9, but for the $IVT_{500-200\ hPa}$ (kg m^{-1} s^{-1}) integrated in the range between 500 and 200 hPa of the troposphere.

During periods 00–03 LT and 04–07 LT, an intensification of $IVT_{500-200\ hPa}$ is observed in well-localized areas on the streams of the transition zone A–A. During these periods, the vector field of $IVT_{500-200\ hPa}$ changes slightly from east to northeast, favoring the intrusion of moisture flows from the Amazon towards the inter-Andean valleys through the ravines. These areas of high intensity of $IVT_{500-200\ hPa}$ coincide with a greater generation of clouds and precipitation on the surface represented by the PEI (figure 4).

Figure 11 shows the moisture budget, which is obtained by the vertically integrated product of specific humidity and horizontal mass convergence. Here, negative values are referred to as moisture flux convergence (MFC), which is related to forced lifting (Zhao *et al.* 2020). During the day, the formation of an MFC strip parallel to the mountain chain on the western side of the Andes is observed (figure 11a). Then, during the course of the day (figure 11a and b), the MFC strip moves towards the inter-Andean valleys due to the fact that the

diurnal winds from the west intensify in the afternoon. The MFC strip coincides with the confluence zones of the westerly and easterly winds at near-surface levels. Likewise, the MFC fringes coincide with the highest PEI value (figure 4b and c). Therefore, it can be pointed out that the regions where the greatest amount of clouds and precipitation are generated respond to the convergence mechanism that produces intense vertical movements of the atmosphere. During night periods, this mechanism is not observed along the Andes mountain range because the westerly winds weaken, and as a consequence, they are completely dominated by the easterly winds. During night periods, well-defined convergence areas over the Amazon and the A–A transition zone show significant rises in air masses in these regions. However, it is not easy to identify the convergence mechanisms in these regions, unlike the Andean regions. Therefore, we selected a small domain (black box, figure 11) to identify the main mechanisms of mesoscale that occur in the A–A transition region.
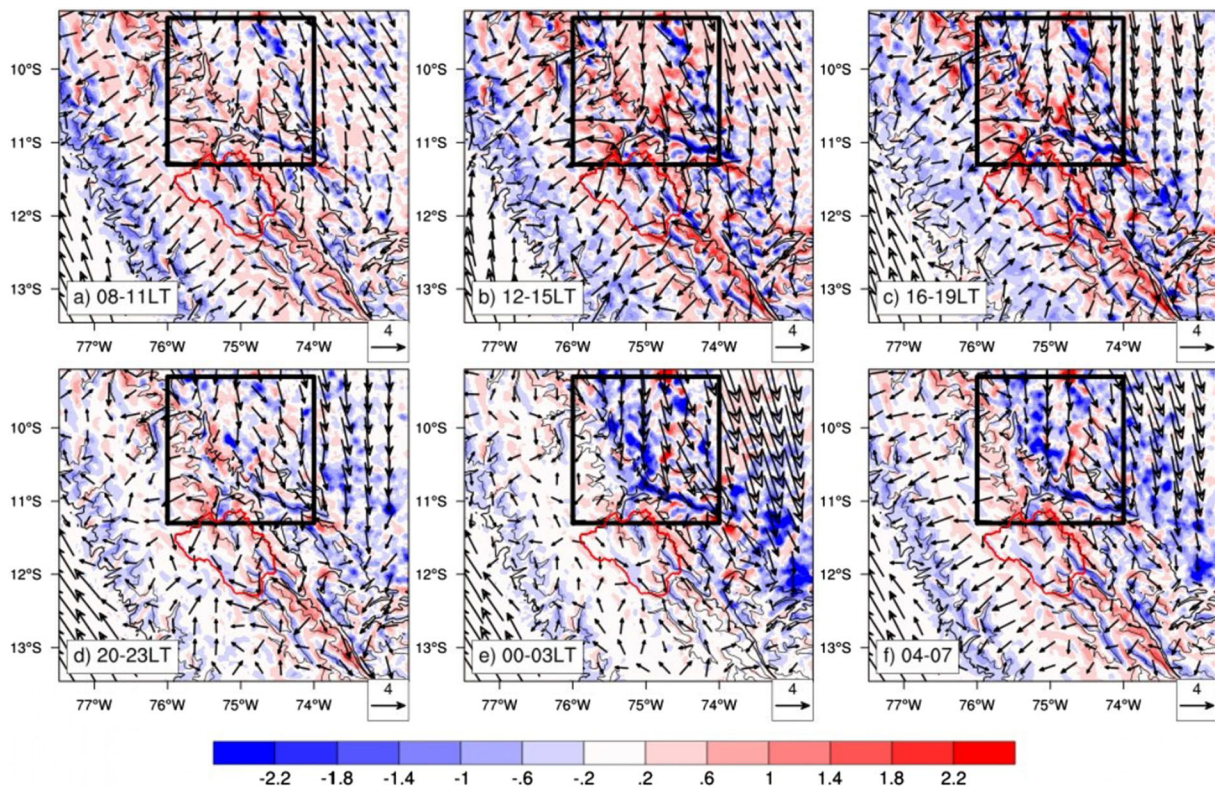

Figure 11. Spatial average of moisture budget from WRF simulations for precipitation events during summer (DJF), negative values (blue) indicate convergence and positive values (red) indicate divergence and have unit: 10^{-5} kg m^{-2} s^{-1}, vector fields are near-surface horizontal winds (m/s). (**a**) 08–11 LT, (**b**) 12–15 LT, (**c**) 16–19 LT, (**d**) 20–23 LT, (**e**) 00–03 LT, and (**f**) 04–07 LT. The height contours at 1000 and 3000 m are provided for reference. A black box will be used to analyze the atmospheric dynamics associated with the PEI hot-spot region and the Andes–Amazon transition region.

Revised Proof

3.5 *Atmospheric dynamics in the A–A transition region*

Figure 12 shows the horizontal wind circulation and its magnitude at 730 hPa focused on the A–A transition region (black rectangle in figure 11). It is observed that the winds are well channeled from the north to the south in regions with low elevations. These winds are associated with low-level jets. The direction of these winds undergoes a significant deviation when they meet the winds coming from the slopes of the A–A transition zone due to the blocking effect of the mountain range. The wind direction is deflected to the east (figure 12b) when it meets the mountain range. This region of strong interaction between the intense winds from the north with the winds from the slopes and the topography of the Andes coincides with the most productive region of clouds and precipitation (black box), mainly at night. During the night, the winds coming from the north intensify their magnitude and, therefore, have a greater capacity to overcome the obstacle of the mountain range (figure 12e). This mesoscale interaction process causes an attenuation effect of the intensity of the winds; the greater this intensity, the attenuation process will also be greater (figure 12e), and as a result, the wind flow only escapes towards higher levels of the tropospheric layer, causing a significant increase in air masses. Around the intense wind flows, horizontal wind magnitude decreases. It is evident that the north wind enters with an increased magnitude and leaves with a reduced magnitude, as seen in figure 12(e). This process is caused by the convergence of winds that are associated with the formation of ascending vertical movements. This behavior of the winds is consistent with the result shown in figure 11(e), which shows the moisture flux convergence patterns during the night.

In figure 13, the moisture flux is shown in three dimensions for levels near the surface. The flow transports water vapor from the north to the south; these flows are intense at levels close to the surface that enter the Andes, particularly entering through a deep ravine known as the Canyon Valley. At 12–15 LT (figure 13a), the flows from the north enter along the Canyon Valley. Likewise, it is observed that the flows are diverted towards the higher slopes of the Andes. These upslope flows are associated with thermal circulations induced by solar radiation that heats the slopes during the day. At 16–19 LT (figure 13b), the same pattern of the previous hours persists, although a slight
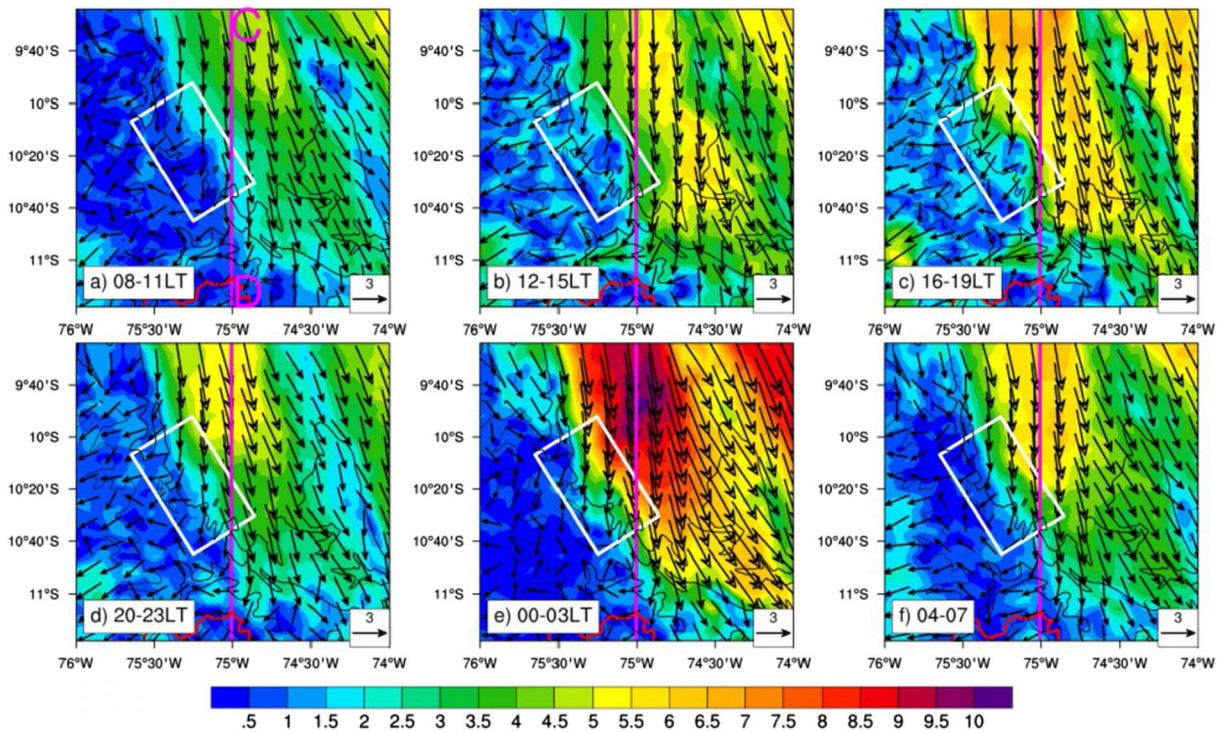

Figure 12. Vector field and magnitude of horizontal winds (m/s) at 730 hPa for the black box in figure 11. The white box represents the PEI hot-spot region (see figure 4f). Line C–D (magenta vertical line) shows the transect along the 75°W longitude for figure 15.
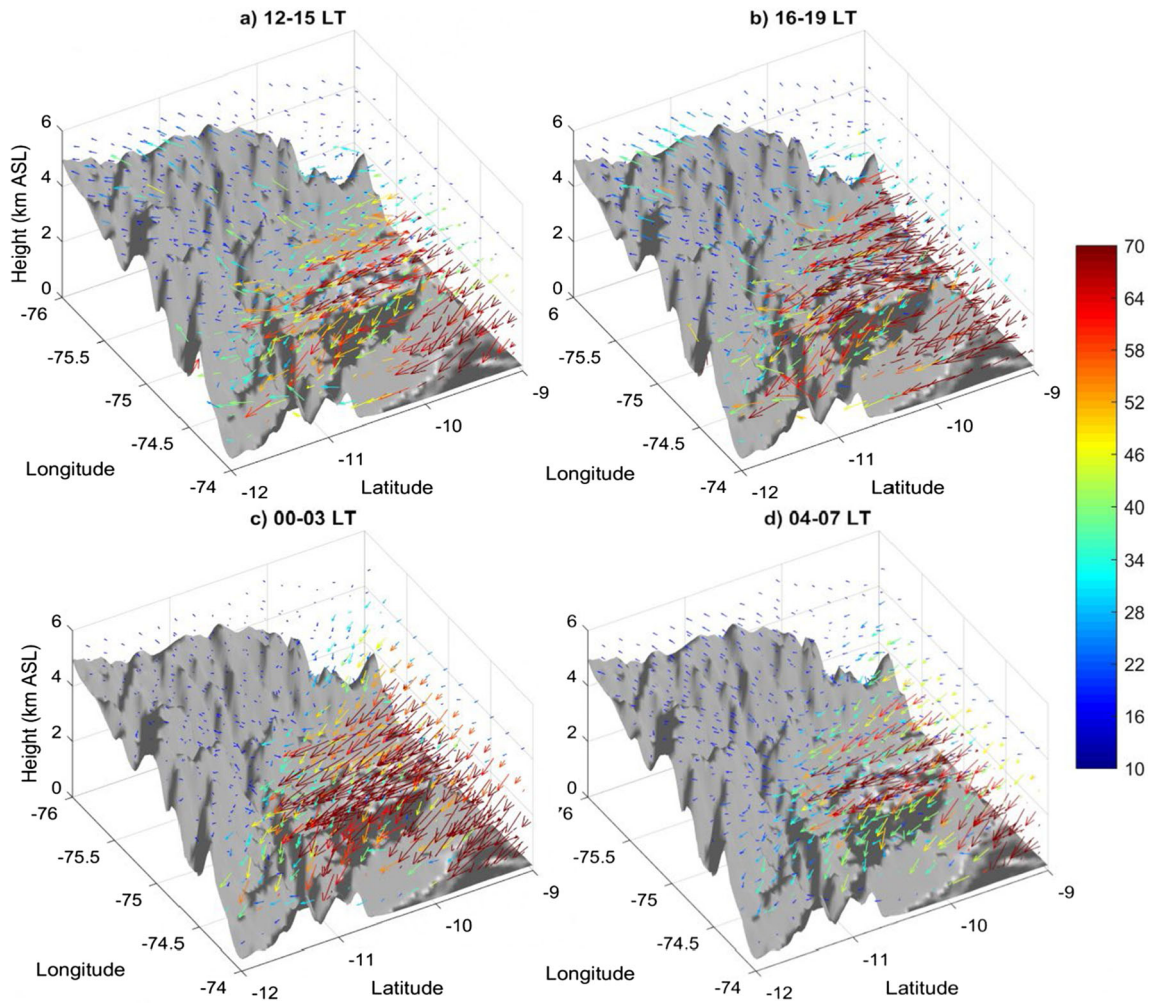
Revised Proof

J. Earth Syst. Sci. _####################_   Page 15 of 24   _####_

Figure 13. Three-dimensional moisture flux (m/s * g/kg) over the A–A transition region averaged over the following local time periods from WRF simulations for precipitation events during summer (DJF), (**a**) 12–15 LT, (**b**) 16–19 LT, (**c**) 00–03 LT, and (**d**) 04–07 LT.

increase in moisture transport towards the A–A transition zone is observed in the higher parts of the Andes.

During the night at 00–03 LT (figure 13c) and 04–07 LT (figure 13d), the flow pattern varies strongly in relation to daytime flows. Especially between 00 and 03 LT, moisture transport increases significantly; although these flows are intense, they do not deviate towards the higher slopes of the Andes. On the contrary, they are channeled by lower levels bordering the contour of the Andes in the A–A transition region, and as they enter the Andes, they decrease in magnitude. With this result, it was evidenced that an important change occurs in the flow patterns between day and night on the higher slopes of the Andes; at night, the intensity of the wind is neutral. From these results, it can be seen that the flows from the north that enter through the Canyon Valley are blocked both

by the topography of the Andes and by the masses of cold air that are located on the higher slopes of the Andes.

Figure 14 shows the vertical profiles of atmospheric variables in the tropospheric column over the PEI hot-spot region in the A–A transition zone. Specifically, vertical averaging of the atmospheric variables within the white box was performed (figure 12). The equivalent potential temperature (Te) that combines both the moisture content and the temperature of the atmosphere shows higher values at levels close to the surface, and its vertical profile changes between daytime and nighttime hours (figure 14a). In the daytime, the values of Te begin with a higher value and then significantly decrease as the height increases. On the other hand, during the night (00–03 LT), the Te increases slightly from the surface to higher levels, and above 800 hPa, the vertical Te gradient decreases
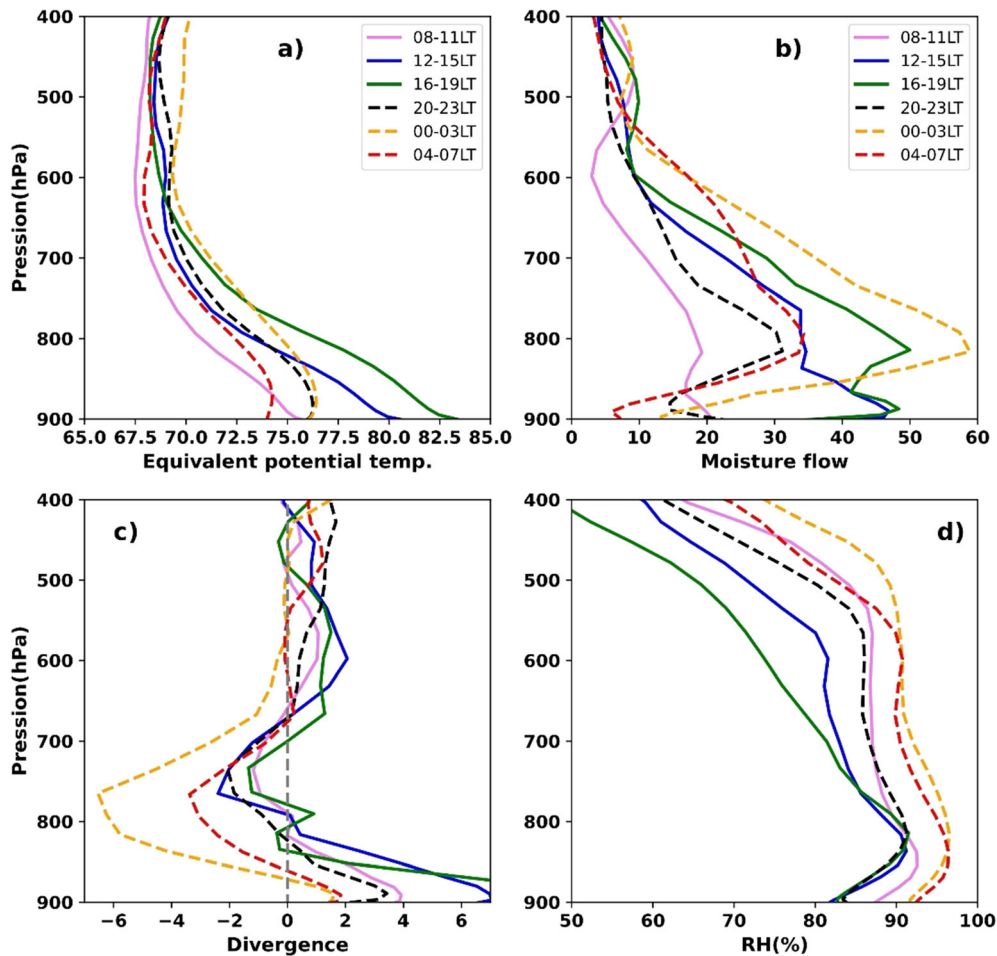
Figure 14. Vertical profiles of atmospheric variables over the PEI hot-spot region (white box in figure 12) from WRF simulations for precipitation events during summer (DJF), (**a**) equivalent potential temperature (K), (**b**) moisture flow (m/s ∗ g/kg), (**c**) moisture flux convergence, and (**d**) relative humidity (%).

slowly; even above 750 hPa, the Te values exceed the diurnal values. At specific times of the day, particularly at night (00–03 LT and 16–19 LT), the flow of moisture increases considerably (figure 14b) at various levels of the tropospheric column, and the flow of water vapor has its maximum intensity level around 800 hPa. Convergence normally occurs at all times during the day (figure 14c), ranging from 850 to 700 hPa, of which the most intense convergence occurs at night (00–03 LT and 04–07 LT). Especially during these times, higher values of relative humidity are observed at various vertical levels (figure 14d). With this result, it is evident that there are favorable atmospheric conditions for the occurrence of intense precipitations and the formation of cumulonimbus clouds associated with the generation of storms due to the presence of convergence of winds and fluxes of humidity that occur mainly at night.

To analyze the ascending vertical circulations of wind fields, a latitudinal section was made on line A–B (as shown in figure 12a). The vertical structure of this section is shown in figure 15. During the period from 08 to 11 LT (figure 15a), the winds come from the north throughout the vertical column of the troposphere, although there is a strip of weak winds above 5 km in height over the Amazon. Over low hills (Lat. = 10.5°S, figure 15a), uphill winds occur with a significant increase in intensity. Also, wind intensity increases in the upper parts of the Andes (Lat. =11.5°S), where an atmospheric disturbance occurs at lower levels. In some cases, this disturbance can be deep, generating atmospheric instability in the middle levels of the troposphere. The disturbances are more notable during the period from 12 to 15 LT, generating a strong atmospheric instability throughout the tropospheric column, especially in the hills and the upper part of the Andes (figure 15b).

The upslope winds are intensified by the thermal effect. During the period from 16 to 19 LT, the northerly winds are quite superficial and

Revised Proof

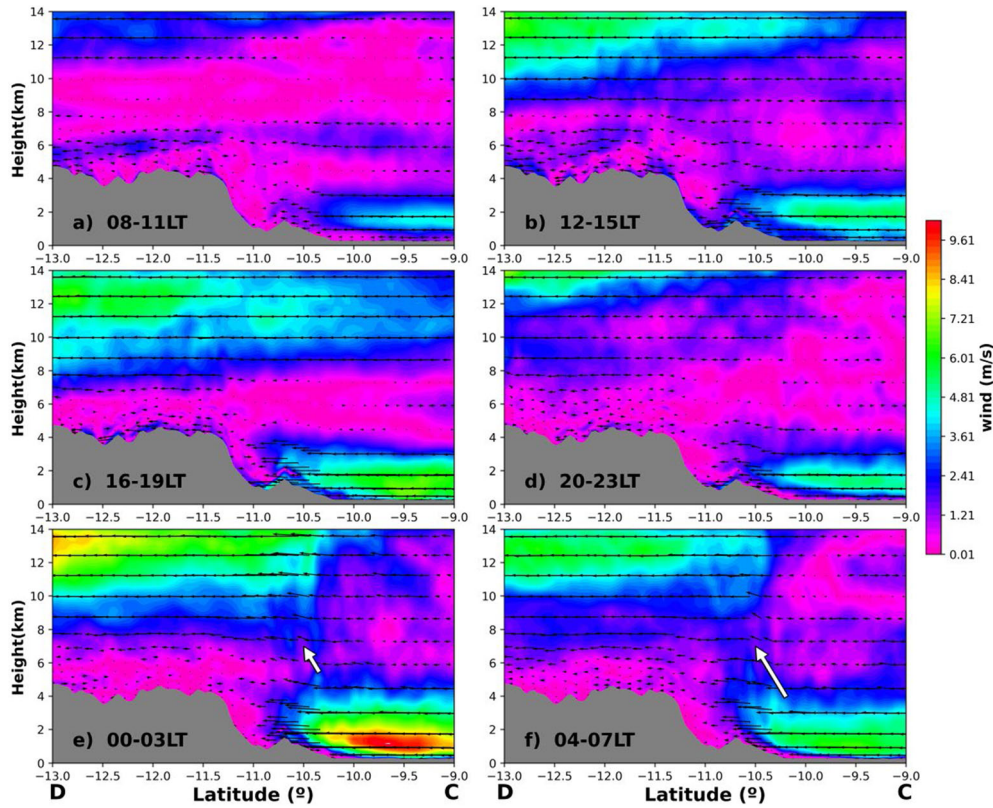*J. Earth Syst. Sci.* _####################_ Page 17 of 24 _####_

Figure 15. Wind cross section (using meridional and vertical components) calculated along the latitude on line C–D (see figure 12) from WRF simulations for precipitation events during summer (DJF), (**a**) 08–11 LT, (**b**) 12–15 LT, (**c**) 16–19 LT, (**d**) 20–23 LT, (**e**) 00–03 LT, and (**f**) 04–07 LT. White vector indicates the intensity of orographic lift.

compressed due to the weak winds that dominate from the opposite direction (south–north) in a specific upper-level layer (5 and 7 km high). During the period from 20 to 23 LT, the layer of weak winds is thicker in the middle level of the troposphere, covering the slopes and the upper parts of the Andes. There are no significant rises in these areas, as observed during daylight hours because the upslope winds disappear at night. On the contrary, downslope winds predominate. In spite of that, atmospheric disturbances are produced on the lower hills, mainly associated with the jets of northerly winds. During the period from 00 to 03 LT, weak winds prevail over the highlands and on the slopes to the east of the Andes, and at surface level, the winds descend, accumulating masses of cold air in the valleys and slopes of the A–A transition zone, due to katabatic circulation. At this time, the winds from the north increase strongly, and they encounter two blocking effects: the topography and the masses of cold air. As a result of this interaction, the winds are redirected towards higher levels, causing atmospheric instability at medium to higher levels of the

troposphere. The same pattern is observed in the later times (04–07 LT) but with lower intensities due to the fact that the magnitude of the northerly winds decreases near the surface.

Figure 16 shows the ascending and descending circulations in the transect to the Andes and the transition zones A–A. At the same time, the equivalent potential temperature contours are shown, which present intense magnitudes in areas close to the surface, and a negative vertical gradient is also observed, which indicates strong conditions of atmospheric instability in a humid condition, especially during periods of 00–03 LT and 04–07 LT. On the contrary, during the day, on the western slopes and high regions of the Andes, upward vertical movements occur associated with upslope winds generated by anabatic circulations (figure 13b). During the night, the ascending circulations are more intense and generalized over the A–A transition zones. They do not respond to anabatic circulations but are associated with the convergence of moisture flows generated by the topographic barrier effect and cold air masses located along the eastern slopes of the Andes.
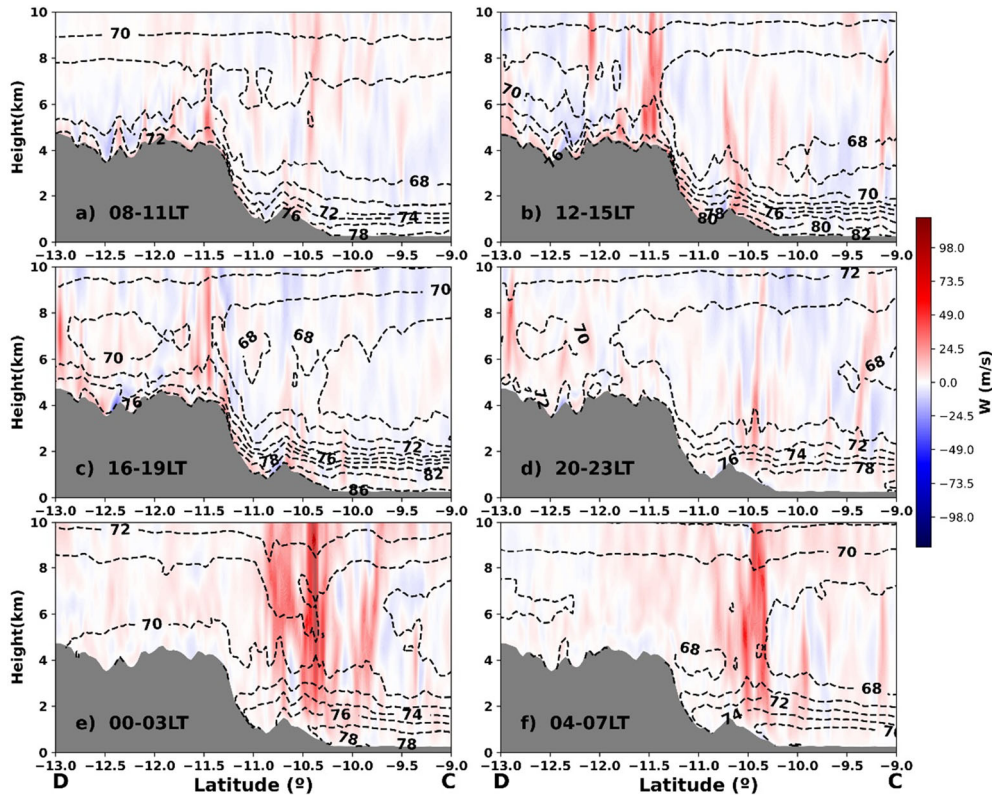
Figure 16. Same as figure 15, but for vertical velocity (w, m/s) and equivalent potential temperature (K). Dashed contours with a label that indicates the values.

4. Discussion

Due to the lack of data on an hourly scale in the study region, it has been impossible to analyze the diurnal cycle of precipitation. However, from daily data (mm/day), annual precipitation was characterized along the Andes transect and over the A–A transition zone. Precipitation patterns present two modes in the transect. The first mode is observed over the western region of the Andes mountain range; in this elevated region, specifically in E3 (4675 m a.s.l.), caution must be taken while recording the pluviometer readings due to the occurrence of solid precipitation (snow). In the Andes, the measurement of solid precipitation currently represents a challenge (Condom *et al.* 2020) since the measured precipitation could be influenced by the melting of snow accumulated in the pluviometer. The second mode is observed in the A–A transition region, where a greater amount of accumulated precipitation was found in relation to the other transect points. Therefore, the A–A transition zone corresponds to the hot-spot precipitation region. The rainfall that occurs in this region has a high variability in its intensity; particularly, its variability is more notable from the median to the most extreme quartiles, which generates a greater accumulation of precipitation (figure 2b). The contributions to annual precipitation in the transition periods (SON and MAM) represent 20% in the inter-Andean valleys and the A–A transition region.

Meanwhile, on the western slopes of the Andes, the contributions differ by 40%, which indicates that seasonal precipitation responds to different atmospheric conditions. For example, during the MAM, the zonal circulation at upper levels is persistent due to the delay in the weakening of Bolivian High, while during the SON, the circulation is dominated by the southern component (Trachte *et al.* 2018). During the rainy months (DJF), the contribution to total precipitation is 60% on the western slopes of the Andes, 53% in the inter-Andean valley, and only 40% in the A–A transition zone.

During the wet season (November–April), the contribution is 70%, which shows that the rainfall that occurs during the dry season (May–September) contributes 30% in the A–A transition zone.

The N-GPM blind zone (Ku band), defined as the atmospheric layer close to the surface that the radar cannot observe, has a pronounced height in

the inter-Andean valleys due to the fact that the radar signal is heavily contaminated by the irregular topography of the Andes. Due to the presence of the blind zone, the radar does not capture the entire column of precipitation clouds, which generates high uncertainty in the quantification of precipitation, as well as in the determination of the bright band over the Andes (Barros and Arulraj 2020; Valdivia *et al.* 2022). Therefore, it is evident that, in the Andes, it is necessary to consider the correction of the blind zone to improve the capture of the complete structure of the cloud system, especially in the inter-Andean ravines.

Tropospheric hydrometeors (LWP and IWP) have different proportions between the Andes region and the A–A transition zone. Over the Andes, the total content of hydrometeors is composed in greater proportion by solid types. This is because the precipitation clouds have a predominant vertical extension above the freezing height. In addition, the freezing height is closer to the surface, which favors the formation of cold clouds. Meanwhile, in the A–A transition zone and the Amazon, liquid-type hydrometeors predominate due to the high amount of cloudiness that forms below the freezing height (Villalobos *et al.* 2019). Also, hydrometeors that are above freezing height are able to change phase from solid to liquid because they have to travel a greater distance to reach the surface.

On a daily scale, the PEI shows a well-defined pattern of the most efficient areas in producing hydrometeors and precipitation. In the A–A transition region, there are more efficient areas with values above 100% PEI, probably because the microphysical process of coalescence predominates below the freezing height (Huang and Chen 2019). These most efficient areas coincide with the precipitation hot-spot regions identified from the TRMM radar data (Espinoza *et al.* 2015a; Chavez and Takahashi 2017). Our results confirm that precipitation hot-spot areas depend to a greater extent on LWP-type hydrometeors and not so much on IWP-type hydrometeors. On an hourly scale, the PEI shows different spatial patterns depending on the diurnal cycle. The mountain chain and the inter-Andean valleys are the most efficient regions in producing hydrometeors and precipitation from noon to the beginning of the night (12–19 LT). During these hours, the PEI depends to a greater extent on IWP and a lesser extent on LWP; that is, there is a greater proportion of solid-type hydrometeors throughout the

tropospheric column. At night, the PEI pattern is inverted since it is observed that the most efficient region in the production of hydrometeors and precipitation is the A–A transition zone, known as the precipitation hot-spot region that occurs from midnight to early morning (00–07 LT). During these hours, the PEI is dominated by clouds and stratiform precipitation, clearly defined by the bright band (figure 5e and f), and that lasts until later hours (figure 4a). Total hydrometeors (PP) have marked patterns between the Andean and A–A transition regions. In the Andean regions, during the most productive hours, the PP does not exceed the values of the A–A transition zone; however, the same does not occur with the PEI values. In the Andean regions, the PEI has higher values than in the A–A transition zone. This behavior of the PEI responds mainly to the stages of convective cloud formation and the abundance of hydrometeors that occur over the Andes. In contrast, the PEI has lower values over the A–A transition region because it is associated with the formation of isolated and localized convective clouds. Subsequently, the PEI increases when the convective clouds reach the dissipation phase (stratiform precipitation), causing an impact on the PEI values.

In the present study, the efficiency of using the PEI is discussed from the dynamic aspect of the atmosphere associated with the production of hydrometeors and precipitation. However, the efficiency of precipitation can be affected by other physical processes, such as the interaction of aerosols–clouds (A–C) and aerosol–radiation (A–R). Both processes can affect the dynamics, thermodynamics, cloud microphysics, and orographic precipitation (Henao *et al.* 2023; Masrour and Rezazadeh 2023). In the Andes of Peru, knowledge about the A–C and A–R processes is limited due to the complexity of these processes and the lack of specialized equipment required to carry out studies. Therefore, in future work, it is necessary to include studies of these processes associated with the efficiency of precipitation, taking into account that the Andes of Peru receive a significant amount of atmospheric aerosols that move from both sides of the Andes: Atlantic flank, including the Amazonia and Pacific flank including the coasts and Pacific Ocean (Moya-Álvarez *et al.* 2023).

Moisture flux patterns are calculated at the surface level (figure 8) and, in turn, integrated into

two layers of the troposphere (figures 9 and 10). On the western slopes of the Andes, $IVT_{sfc-500\ hPa}$ intensifies in conjunction with surface flows, especially in the afternoon. These flows transport water vapor perpendicular to the Andes mountain range from the Pacific side due to mesoscale thermal circulation and are probably strengthened by sea breezes from the Pacific Ocean (Moya-Álvarez *et al.* 2020; Flores-Rojas *et al.* 2021). In contrast, on the eastern slopes of the Andes, the $IVT_{sfc-500\ hPa}$ associated with low-level jets from the Amazon is channeled into the A–A transition region and the inter-Andean valleys through the lower region known as the Canyon Valley (75.3°W, 9.5°S), generating the conditions for the formation of clouds and precipitation (Kumar *et al.* 2019; Chavez *et al.* 2020). $IVT_{500-200\ hPa}$ prevails with the easterly circulation during the diurnal cycle, instead its magnitude patterns change considerably. During the day, there is a notable increase in the transport of water vapor on both sides of the slopes of the Andes (leeward and windward). At night, there is greater transport of water vapor only in focused areas, for example, in the most efficient regions of hydrometeors and precipitations of the A–A transition zone.

Based on the analyzed results, a scheme of atmospheric circulation mechanisms at the mesoscale level is proposed (figure 17) that are key in the development of clouds and intense precipitation in the central Andes of Peru and the A–A transition regions. During the day, precipitation clouds develop associated with the increased upslope circulation that predominates on both sides of the Andean slopes. During the day, these clouds reach their mature phase, leading to increased transport of water vapor. This causes moisture to enter the inter-Andean valleys from both the Pacific side and the Amazon (Martínez-Castro *et al.* 2019; Flores-Rojas *et al.* 2021). The same pattern of circulations and moisture flows was reported in the Santa River basin (latitude 9.5°S) (Rosales *et al.* 2022).

The circulation from the east intensifies in the inter-Andean valleys, and when they meet the circulation from the west, both converge along the Andes mountain range. As a result of this convergence, a chain of convective multicells is formed with high concentrations of hydrometeors that produce intense precipitation. This circulation mechanism was evidenced in case studies during intense convective precipitation events in the Mantaro Valley (Martínez-Castro *et al.* 2019;

Flores-Rojas *et al.* 2021). This convergence strip moves transversally towards the inter-Andean valleys due to the fact that the circulation from the west intensifies in relation to those from the east as the hours of the day advance. Especially during the afternoon hours (figure 17a), the convergence zones represent more efficient areas in producing precipitation particles, mainly composed of solid-phase hydrometeors and intense precipitation on the surface.

At night, atmospheric circulation patterns change relative to daytime patterns. The circulation from the north associated with low-level jets (below 4 km high) increases their magnitude significantly. As you enter the A–A transition region, you encounter two well-defined barriers: the topography of the Andes and the masses of cold air located in the highlands and slopes to the east of the Andes. Due to the notable increase in the northerly circulation and its interaction with the topographical barrier and cold air masses, an atmospheric convergence develops over the A–A transition region (Giovannettone and Barros 2009; Espinoza *et al.* 2015a; Chavez and Takahashi 2017). Therefore, the A–A transition region is characterized as the most efficient area in producing hydrometeors, composed of a higher fraction of liquid-phase hydrometeors and surface precipitation, which occur during night periods. Instead, overnight significant precipitation does not develop over the Andes because the circulation from the east is intense and dominates the circulation from the west, mainly at lower levels of the troposphere.

The mesoscale atmospheric modeling used in this study was able to identify the main thermal circulation mechanisms to explain the most efficient areas of hydrometeor and precipitation production in the Andean regions and the A–A transition zone. The selected precipitation events from the N-GPM satellite are representative of the summer (DJF) of the period 2014–2022 and have statistical significance with a confidence level of 95%. To explain the local processes related to the most efficient areas of precipitation production, it is necessary to carry out simulations with a high spatial resolution, as has been done in other places in the tropical Andes (Junquas *et al.* 2018; Ruiz-Hernández *et al.* 2021; Rosales *et al.* 2022). Likewise, numerical experiments must be carried out modifying the topography of the most efficient areas in the production of precipitation that were identified in this study and in the regions through which the flow of humidity is channeled to understand the local

Revised Proof

J. Earth Syst. Sci. _###################_   Page 21 of 24   _####_
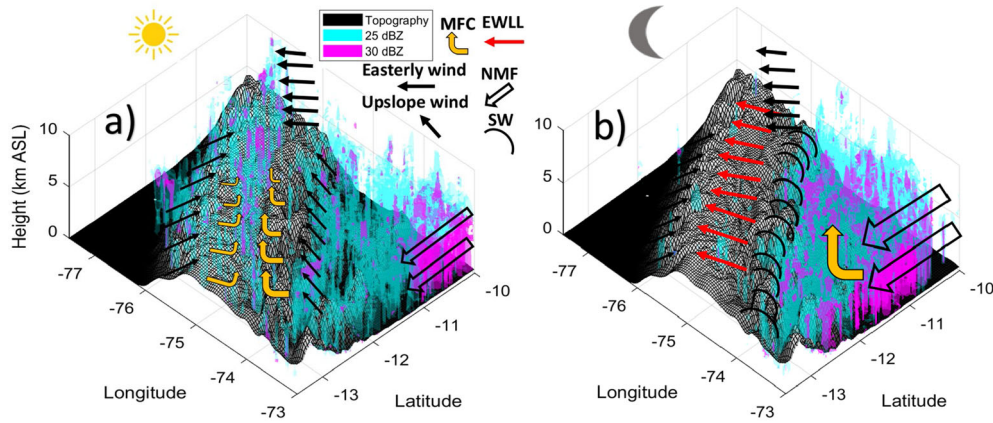
Figure 17. Conceptual diagram of the mesoscale circulations that predominate during precipitation in the Andes–Amazon region of central Peru. The precipitating cloud system is represented in three dimensions through 25 dBZ (cyan) and 30 dBZ (magenta) thresholds estimated by the N-GPM satellite. (**a**) During the day, upslope winds predominate on both sides of the Andes, and the interior of the Andes experiences moisture flux convergence (MFC, wide yellow arrows). (**b**) During the night, convergence does not occur over the Andes because the easterly low-level winds (EWLL, red arrows) dominate the westerly winds. Over the high elevations and slopes to the east of the Andes, the air mass is characterized by cold and stable wind (SW, black curved lines). These air masses and the topography of the Andes block the northerly flows (NMF, black outlines arrows) propagating from a region of MFC centered on the Andes–Amazon transition zone.

interaction that occurs between these moisture flows and the topography.

5. Conclusions

This study presents the diurnal cycle analysis of the total availability of tropospheric hydrometeors and their associated atmospheric patterns over the connected Andes–Amazon system of the central region of Peru. The total number of hydrometeors was analyzed at the diurnal cycle level using the N-GPM radar data for the period 2014–2022, while the atmospheric dynamics were analyzed using the hourly outputs of the WRF regional model. Due to the high computational cost, only a total of 120 numerical simulations corresponding to randomly selected precipitation events were carried out among all the events detected by the N-GPM satellite radar. Based on the results obtained, a scheme of atmospheric circulation patterns that predominate during the hours of greatest production of tropospheric hydrometeors and precipitation at the surface level is proposed (figure 17). The conclusions of this work are the following:

- The seasonal and annual accumulated precipitation presents two modes on the A–A transect. The first occurs on the Andes mountain range caused by the prevailing atmospheric circulations during daytime hours. The second mode is more pronounced compared to the previous one and is generated on the A–A

transition zone forced by the prevailing atmospheric circulations during the night hours.

- The difference in total content and type of tropospheric hydrometeors is well-marked between the Andes and the A–A transition zone. Over the Andean region, they are composed of a greater proportion of solid-type hydrometeors, and over the A–A region, they are composed of a greater proportion of liquid-type hydrometeors.
- The efficiency of extracting precipitation from tropospheric hydrometeors has opposite diurnal behavior in the transect to the Andes and the A–A transition zone. During the period from 16–19 LT, a positive gradient (west–east) of efficiency is generated over the transect, the Andes mountain range being the most efficient area to extract hydrometeors as precipitation at the surface level. On the other hand, during the period from 04–07 LT, a negative gradient (east–west) of efficiency is generated over the transect, the transition zone A–A being the most efficient area to extract hydrometeors as precipitation at the surface level.

In addition, two patterns of atmospheric circulations at the mesoscale level were identified that are predominant during the most efficient hours of production of hydrometeors and precipitation on the surface, which are the following:

- During the daytime, early in the morning, orographic clouds develop over the mountains due to the effect of the upslope winds that

predominate on both slopes of the Andes. Over the course of the day, these clouds develop into the mature phase due to the convergence of horizontal winds from the west and east over the Andes mountain range. The convergence strip, formed by a chain of convective multicells, moves transversally from the Andes mountain range towards the inter-Andean valleys due to the intensification of the thermal circulation from the west in relation to that from the east.

- At night, the circulation from the north associated with the low-level jet increases notably. Upon entering the A–A transition zone, it encounters two well-defined barriers: the topography and the masses of cold air located on slopes and high areas of the eastern flank of the Andes. The A–A transition zone is characterized by the fact that the convergence process predominates due to the change in the magnitude of the northerly horizontal winds that enter with greater intensity and leave with lower intensities. Consequently, ascending vertical movements are generated, which generate deep convection and produce intense precipitation.

Acknowledgements

Author Statement

EVP: Conceptualization, Methodology, Software, writing-original draft preparation, AM: Investigation, Writing- Reviewing and Editing, DMC: Validation, Investigation, Conceptualization, JV: Methodology, Investigation, Data curation, RCV: Investigation, Validation, Conceptualization, WLC: Investigation, Validation, AS: Investigation, Validation, Software.

References

Aybar C, Fernández C, Huerta A, Lavado W, Vega F and Felipe-Obando O 2020 Construction of a high-resolution gridded rainfall dataset for peru from 1981 to the present day; *Hydrol. Sci. J.* **65(5)** 770–785.

Barros A P and Arulraj M 2020 Remote sensing of orographic precipitation; In: *Satellite Precipitation Measurement* **2** 559–582, https://doi.org/10.1007/978-3-030-35798-6_6.

Castillo-Velarde D, Kumar S, Valdivia-Prado J M, Moya-Álvarez A S, Flores-Rojas J L, Villalobos-Puma E, Martínez-Castro D and Silva-Vidal Y *et al.* 2021 Evaluation of GPM dual-frequency precipitation radar algorithms to estimate drop size distribution parameters, using ground-based measurement over the central Andes of Peru; *Earth Syst. Environ.* **5(3)** 597–619, https://doi.org/10.1007/s41748-021-00242-5.

Chávez S and Takahashi K 2017 Orographic rainfall hot spots in the Andes–Amazon transition according to the TRMMM precipitation radar and *in situ* data; *J. Geophys. Res. Atmos.* **122**, https://doi.org/10.1002/2016JDO26282.

Condom T, Martínez R, Pabo´n J D, Costa F, Pineda L, Nieto J J, López F and Villacis M 2020 Climatological and hydrological observations for the South American Andes: *In situ* stations, satellite, and reanalysis data sets; *Front. Earth Sci.* **8** 92, https://doi.org/10.3389/feart.2020.00092.

Espinoza J, Chavez S, Ronchail J, Junquas C, Takahashi K and Lavado W 2015a Rainfall hotspots over the southern tropical Andes: Spatial distribution, rainfall intensity and relations with large-scale atmospheric circulation; *Water Resour. Res.* **51** 1–17, https://doi.org/10.1002/2014WR016273.

Espinoza J C, Chavez S, Ronchail J, Junquas C, Takahashi K and Lavado W 2015b Rainfall hotspots over the southern tropical Andes: Spatial distribution, rainfall intensity, and relations with large-scale atmospheric circulation; *Water Resour. Res.* **51(5)** 3459–3475, https://doi.org/10.1002/2014WR016273.

Flores-Rojas J L, Moya-Álvarez A S, Valdivia-Prado J M, Piñas-Laura M, Kumar S, Karam H A, Villalobos-Puma E, Martínez-Castro D and Silva Y 2021 On the dynamic mechanisms of intense rainfall events in the central Andes of Peru, Mantaro valley; *Atmos. Res.* **248** 105188, https://doi.org/10.1016/j.atmosres.2020.105188.

Giovannettone J P and Barros A P 2009 Probing regional orographic controls of precipitation and cloudiness in the central Andes using satellite data; *J. Hydrometeorol.* **10(1)** 167–182, https://doi.org/10.1175/2008JHM973.1.

Henao J J, Mejia J F and McDonough F 2023 Impacts of anthropogenic aerosols on orographic precipitation in Arizona; *Urban Clim.* **49** 101561.

Hou A Y, Kakar R K, Neeck S, Azarbarzin A A, Kummerow C D, Kojima M, Oki R, Nakamura K and Iguchi T 2014 The global precipitation measurement mission; *Bull. Am. Meteorol. Soc.* **95(5)** 701–722, https://doi.org/10.1175/BAMS-D-13-00164.1.

Revised Proof

Huang H and Chen F 2019 Precipitation microphysics of tropical cyclones over the western north pacific based on GPM DPR observations: A preliminary analysis; *J. Geophys. Res.: Atmos.* **124(6)** 3124–3142, https://doi.org/10.1029/2018JD029454.

Junquas C, Takahashi K, Condom T, Espinoza J, Chavez S, Sicart J and Lebel T 2018 Understanding the influence of orography on the precipitation diurnal cycle and the associated atmospheric processes in the central Andes; *Clim. Dyn.* **50** 3995–4017, https://doi.org/10.1007/s00382-017-3858-8.

Kumar S, Vidal Y S, Moya-Álvarez A S and Martínez-Castro D 2019 Effect of the surface wind flow and topography on precipitating cloud systems over the Andes and associated amazon basin: GPM observations; *Atmos. Res.* **225** 193–208, https://doi.org/10.1016/j.atmosres.2019.03.027.

Liao L and Meneghini R 2022 GPM DPR retrievals: Algorithm, evaluation, and validation; *Remote Sens.* **14(4)** 843, https://doi.org/10.3390/rs14040843.

Martínez-Castro D, Kumar S, Flores-Rojas J L, Moya-Álvarez A, Valdivia-Prado J M, Villalobos-Puma E, Castillo-Velarde C D and Silva-Vidal Y 2019 The impact of microphysics parameterization in the simulation of two convective rainfall events over the central Andes of Peru using WRF-ARW; *Atmosphere* **10(8)** 442, https://doi.org/10.3390/atmos10080442.

Masrour P F and Rezazadeh M 2023 Aerosol-cloud-precipitation interaction during some convective events over southwestern Iran using the WRF model; *Atmos. Pollut. Res.* **14(2)** 101667.

Moya-Álvarez A, Martínez-Castro D, Flores-Rojas J and Silva-Vidal Y 2018 Sensitivity study on the influence of parameterization schemes in WRF-ARW model on short- and medium-range precipitation forecasts in the central Andes of Peru; *Adv. Meteorol.* **2018** 1381092, https://doi.org/10.1155/2018/1381092.

Moya-Álvarez A, Martínez-Castro D, Kumar S and Silva Y 2019 Response of the WRF model to different resolutions in the rainfall forecast over the complex Peruvian orography; *Theor. Appl. Climatol.* **137** 2993, https://doi.org/10.1007/s00704-019-02782-3.

Moya-Álvarez A, Martínez-Castro D, Kumar S, Flores-Rojas J, Estevan R, Saavedra-Huanca M and Silva Y 2020 Statistical characterization of vertical meteorological profiles obtained with the WRF-ARW model on the central Andes of Peru and its relationship with the occurrence of precipitation on the region; *Atmos. Res.* **239** 104915, https://doi.org/10.1016/j.atmosres.2020.104915.

Moya-Álvarez A S, Estevan R, Martínez-Castro D and Silva Y 2023 Spatial and temporal distribution of black carbon in Peru from the analysis of biomass burning sources and the use of numerical models; *Earth Syst. Environ.* **7** 411–430.

Myers N, Mittermeier R A, Mittermeier C G, da Fonseca G A and Kent J 2000 Biodiversity hotspots for conservation priorities; *Nature* **403(6772)** 853–858, https://doi.org/10.1038/35002501.

Rosales A G, Junquas C, da Rocha R P, Condom T and Espinoza J C 2022 Valley–mountain circulation associated with the diurnal cycle of precipitation in the tropical Andes (Santa river basin, Peru); *Atmosphere* **13(2)** 344, https://doi.org/10.3390/atmos13020344.

Ruiz-Hernández J C, Condom T, Ribstein P, Le Moine N, Espinoza J C, Junquas C, Villacís M, Vera A, Muñoz T, Maisincho L *et al.* 2021 Spatial variability of diurnal to seasonal cycles of precipitation from a high altitude equatorial Andean valley to the Amazon basin; *J. Hydrol.: Reg. Stud.* **38** 100924, https://doi.org/10.1016/j.ejrh.2021.100924.

Satyamurty P, da Costa C P W and Manzi A O 2013 Moisture source for the Amazon basin: A study of contrasting years; *Theor. Appl. Climatol.* **111(1)** 195–209, https://doi.org/10.1007/s00704-012-0637-7.

Segura H, Espinoza J C, Junquas C, Lebel T, Vuille M and Garreaud R 2020 Recent changes in the precipitation-driving processes over the southern tropical Andes/western Amazon; *Clim. Dyn.* **54(5)** 2613–2631, https://doi.org/10.1007/s00382-020-05132-6.

Seto S, Iguchi T and Oki T 2013 The basic performance of a precipitation retrieval algorithm for the global precipitation measurement mission's single/dual-frequency radar measurements; *IEEE Trans. Geosci. Remote Sens.* **51(12)** 5239–5251, https://doi.org/10.1109/TGRS.2012.2231686.

Sierra J P, Junquas C, Espinoza J C, Segura H, Condom T, Andrade M, Molina-Carpio J, Ticona L, Mardoñez V and Blacutt L *et al.* 2022 Deforestation impacts on Amazon-Andes hydroclimatic connectivity; *Clim. Dyn.* **58(9)** 2609–2636, https://doi.org/10.21203/rs.3.rs-600041/v1.

Skamarock W C, Klemp J B, Dudhia J, Gill D O, Liu Z, Berner J, Wang W, Powers J G, Duda M G, Barke D M *et al.* 2019 *A description of the advanced research WRF model*; version 4, National Center for Atmospheric Research: Boulder, CO, USA, 145, https://doi.org/10.5065/1dfh-6p97.

Sui C H, Satoh M and Suzuki K 2020 Precipitation efficiency and its role in cloud-radiative feedbacks to climate variability; *J. Meteorol. Soc. Jpn. Ser. II*, https://doi.org/10.2151/jmsj.2020-024.

Trachte K, Seidel J, Figueroa R, Otto M and Bendix J 2018 Cross-scale precipitation variability in a semiarid catchment area on the western slopes of the central Andes; *J. Appl. Meteorol. Climatol.* **57(3)** 675–694, https://doi.org/10.1175/JAMC-D-17-0207.1.

Valdivia J M, Gatlin P N, Kumar S, Scipión D, Silva Y and Petersen W A 2022 The GPM-DPR blind zone effect on satellite-based radar estimation of precipitation over the Andes from a ground-based ka-band profiler perspective; *J. Appl. Meteorol. Climatol.* **61(4)** 441–456, https://doi.org/10.1175/JAMC-D-20-0211.1.

Villalobos E E, Martinez-Castro D, Kumar S, Silva Y and Fashe O 2019 Estudio de tormentas convectivas sobre los Andes centrales del Perú usando los radares PR-TRMM y KuPR-GPM; *Rev. Cuba. Meteorol.* **25(1)** 59–75, http://rcm.insmet.cu/index.php/rcm/article/view/454.

Villalobos-Puma E, Martinez-Castro D, Flores-Rojas J, Saavedra M and Silva Vidal Y 2020 Diurnal cycle of raindrops size distribution in a valley of the Peruvian central Andes; *Atmosphere* **11**, https://doi.org/10.3390/atmos11010038.

Revised Proof

Zhao Y, Chen D, Li J, Chen D, Chang Y, Li J and Qin R 2020 Enhancement of the summer extreme precipitation over North China by interactions between moisture convergence and topographic settings; *Clim. Dyn.* **54(5)** 2713–2730, https://doi.org/10.1007/s00382-020-05139-z.

Corresponding editor: Parthasarathi Mukhopadhyay